



**POLITECNICO  
DI TORINO**

**POLITECNICO DI TORINO**

**Corso di Laurea Magistrale in Ingegneria energetica e nucleare**

**Tesi di Laurea**

**Model to study the expansion of plasma contactor  
emitted by a magnetospheric spacecraft  
to mitigate charging effects**

**Candidata**

**Claudia Colandrea**

**Relatori**

prof. Gianni Coppa (DET)

dr. Gian Luca Delzanno (Los Alamos National Laboratory)

**Anno Accademico 2017-2018**



*A nonna Elia*

# Sommario

L'oggetto di questa tesi si colloca all'interno dello studio di metodi di mitigazione per l'accumulo di carica su sistemi spaziali.

Su di un satellite viene depositata una carica netta diversa da zero, quando sussiste una differenza di potenziale tra esso e l'ambiente circostante.

Dalla letteratura scientifica è noto che l'accumulo di carica causa diversi tipi di danneggiamento al mezzo spaziale e può perfino compromettere l'intera missione. Secondo la National Aeronautics and Space Administration (NASA), l'analisi dell'accumulo di carica e di sistemi di attenuazione di tale fenomeno, richiede ulteriori sviluppi, nonostante varie strategie di mitigazione siano state proposte negli scorsi decenni.

L'indagine condotta nel presente lavoro di tesi si focalizza su una particolare applicazione spaziale: viene affrontato il problema dell'accumulo di carica in un satellite che emette un fascio di elettroni nella magnetosfera. Gli elettroni del fascio si muovono lungo una linea del campo magnetico terrestre, fino a colpire la ionosfera. Durante il loro cammino essi creano un fascio luminoso che permette di stabilire una connessione tra la zona della magnetosfera in cui si trova il satellite e la regione della ionosfera raggiunta.

In tale assetto, il satellite viene caricato positivamente, in quanto gli elettroni emessi portano con sé una carica negativa proporzionale alla potenza del fascio stesso. Il sistema richiede perciò uno schema di mitigazione; nel caso in esame, per eliminare la carica in eccesso dal mezzo spaziale, viene utilizzato un plasma ad alta densità, emesso prima e durante l'iniezione nello spazio del fascio elettronico. Viene proposto dunque un modello numerico per simulare il transitorio durante il quale il plasma si espande; viene infine seguito un approccio semi-analitico.

The goal of this thesis concerns the charging mitigation of a spacecraft that emits a high-power electron beam in the magnetosphere.

Reports in the scientific literature suggest that the hazards caused by spacecraft charging are diverse, potentially compromising a space mission. Therefore, NASA identifies the impact of spacecraft charging as an area that needs further development. Charging mitigation strategies are similarly expanding: different technologies have been designed to get rid of excess electric charge on the space probe and to minimize that of the most severe spacecraft charging. Various charge control systems have been proposed and developed in past decades to find a suitable solution for spacecraft charging, in both steady-state and transient conditions.

Amongst recent active space experiments, the application under study involves the utilization of an electron beam fired from a magnetospheric spacecraft. The beam shot from an electron gun is used to track the magnetic field line along which electrons move, until they strike the ionosphere. This respective electron beam allows for the determination of the ionospheric footprint of the specific magnetosphere region in which the satellite is placed. This configuration is finally aimed to clarify the longstanding issue of magnetosphere-ionosphere coupling.

On the other hand, after its emission, the electron beam leaves behind a positive charge, resulting in high charging potentials of the satellite if a mitigation system is not employed.

To overcome this charging problem, a mitigation method based on the emission of a high-density plasma is adopted. At first, the spacecraft emits the plasma only; in the second stage plasma and electron beam emissions are simultaneous.

The spacecraft transient is simulated via computer modeling for which both numerical and analytical approaches model the physical system in its early phase of the transient, when the plasma shot from the satellite expands in the low-density magnetosphere.

# Contents

<b>List of Tables</b>	VIII
<b>List of Figures</b>	IX
<b>1 Introduction</b>	1
1.1 Solar Wind, Ionosphere and Magnetosphere	1
1.2 Implications of Magnetosphere-Ionosphere Coupling	3
1.2.1 Ionospheric Signatures	3
1.2.2 A possible solution for MI coupling understanding	5
1.3 Spacecraft charging	6
1.3.1 Cause and effects	7
1.3.2 Mitigation	9
<b>2 Theoretical model for the transient of a magnetospheric spacecraft emitting a high-power electron beam</b>	11
2.1 Spacecraft charging mitigation scheme	11
2.1.1 Spacecraft charging equation	11
2.1.2 Electron beam balanced by ion beam	13
2.1.3 Plasma contactor	15
2.1.4 CONNEX	16
2.2 Theoretical model	17
2.2.1 Basic assumptions	18
2.2.2 Normalization	20
2.2.3 Model equations	21
<b>3 Shell model for expansion of contactor plasma</b>	27
3.1 Algorithm	27
3.2 A simpler formulation of the method	29
3.3 Shell method for contactor expansion simulation	29
3.3.1 Initial distribution	29
3.3.2 Time evolution	32

3.3.3	Electric field . . . . .	33
3.3.4	Potential . . . . .	33
3.3.5	Charge Density . . . . .	35
3.4	Shell method convergence study . . . . .	36
3.4.1	Time discretization . . . . .	37
3.4.2	Number of shells . . . . .	42
3.5	CPIC -Shell simulations parallelism . . . . .	46
3.6	Scaling Law for Spacecraft Potential . . . . .	52
3.6.1	Power law approximation . . . . .	54
3.6.2	Polynomial approximation . . . . .	54
3.7	Shell method for beam emission regime . . . . .	57
<b>4</b>	<b>Semi-analytical model for expansion of contactor plasma</b>	<b>61</b>
4.1	Basic assumptions . . . . .	61
4.2	Model equations . . . . .	62
4.2.1	Numerical example . . . . .	66
<b>5</b>	<b>Conclusions</b>	<b>69</b>
	<b>Bibliography</b>	<b>71</b>

# List of Tables

1.1	Altitude classification of various Earth orbits . . . . .	8
2.1	Normalized variables . . . . .	20
3.1	Input data . . . . .	36
3.2	Input time steps for convergence study . . . . .	37
3.3	Input number of shells for convergence study . . . . .	42
3.4	Summary of results in CPIC and shell method simulation . . . . .	46
3.5	End expansion time inputs . . . . .	52
3.6	Ion contactor current inputs . . . . .	53
3.7	Results for case <i>I</i> . . . . .	53
3.8	Results for case <i>II</i> . . . . .	53
3.9	Results for case <i>III</i> . . . . .	53
3.10	Power law approximation results . . . . .	54
3.11	Polynomial approximation results . . . . .	55
4.1	Input data of numerical example . . . . .	66

# List of Figures

1.1	Earth’s magnetosphere and solar wind sketch . . . . .	2
1.2	A view of the aurora australis taken by the Imager for Magnetopause-to-Aurora Global Exploration (IMAGE) spacecraft on January 2005 . . . . .	4
1.3	Northern Lights over Alaska in the night of February 16,2017, Poker Flat Research Range, Fairbanks [5]. . . . .	4
1.4	Potential of a charged spacecraft. Since the spacecraft potential differs from ambient potential, a sheath around it is formed. The plasma inside the sheath is nonneutral [2]. . . . .	6
2.1	Sketch of CONNEX spacecrafts and spot of electron beam traveling along a magnetic field line [22]. . . . .	17
2.2	Reference geometry of semy-analytical model: spacecraft ( <i>dark grey</i> ), quasi-neutral region ( <i>cyan</i> ), ion region ( <i>yellow</i> ), vacuum ( <i>gray</i> ). . . . .	19
3.1	Example of a particle entering from the left boundary of a rectangular spatial grid with velocity $v_r$ . . . . .	30
3.2	Shells sorted according to $r$ in increasing order. . . . .	34
3.3	Convergence study plots varying time step $d\tau$ . . . . .	41
3.4	Convergence study plots varying number of shells $\Delta N_s$ . . . . .	45
3.5	Potential space distribution at different time instants . . . . .	48
3.6	Potential distribution in space at the end of expansion . . . . .	49
3.7	Spacecraft potential time evolution. . . . .	49
3.8	Total charge accumulated on the spacecraft. . . . .	50
3.9	Zoom of total charge accumulated on the spacecraft . . . . .	50
3.10	Density profiles at the end of expansion . . . . .	51
3.11	Best fit of spacecraft potential values (case <i>I</i> ) . . . . .	55
3.12	Best fit of spacecraft potential values (case <i>II</i> ) . . . . .	56
3.13	Best fit of spacecraft potential values (case <i>III</i> ) . . . . .	56
3.14	Time evolution of spacecraft potential during the beam emission . . . . .	58
3.15	Density distribution in space during the beam emission . . . . .	58
3.16	Potential spatial distribution at the end of the transient . . . . .	59
4.1	Charge accumulated on the spacecraft in time . . . . .	67
4.2	Potential distribution in space at the end of expansion . . . . .	67
4.3	Ion density profile in space at the end of expansion . . . . .	68



# Chapter 1

## Introduction

A satellite emitting a high-power electron beam experiences a charge build-up. Spacecraft charging arises whenever the satellite potential differs from the potential of the surrounding energetic environment. Different approaches have been developed to solve this issue and are discussed in the following work.

Before entering in detail of the main topic, some introductory notions are given, in order to understand the merit of such scientific researches and applications.

We start from a brief description of plasma environment around Earth.

### 1.1 Solar Wind, Ionosphere and Magnetosphere

Earth is enveloped by the atmosphere, whose upper layer, the *ionosphere*, is made of partially ionized gas surrounded by a high-density cloud of neutral gas.

The ionosphere lies as the interface between the atmosphere and the magnetosphere.

Earth's *magnetosphere* is the plasma region around our planet in which the terrestrial magnetic field exerts its influence on the motion of charged particles.

In the solar system, magnetospheres of celestial bodies are perturbed by *solar wind*, a stream of charged particles flowing outward from the upper atmosphere of the sun, known as the corona. Furthermore, the structure of the magnetosphere is affected by an interplay between solar wind particles and charged particles originating in the upper layers of Earth's atmosphere.

The outer boundary of the magnetosphere is the *magnetotail*.

Solar wind sweeps supersonically toward the Earth at speeds of  $\sim 400$  km/s, dragging with it a weak magnetic field ( $B \simeq 0.5$  nT). The component of the solar magnetic field that is carried from the corona by solar wind is identified as the Interplanetary Magnetic Field (IMF).

When the solar wind encounters the magnetic field of Earth, a supersonic shock wave is created sunward of Earth, and a bow shape boundary forms, known as the Bow Shock.

Kinetic pressure of solar wind compresses the magnetosphere sunward side to a distance of 6 to 10 times the Earth's radius; the night-side magnetosphere is stretched to 1000 times Earth's radius. The dipolar terrestrial magnetic field is compressed on the dayside as well, and it is dragged on the nightside, forming a tail-like structure [1].

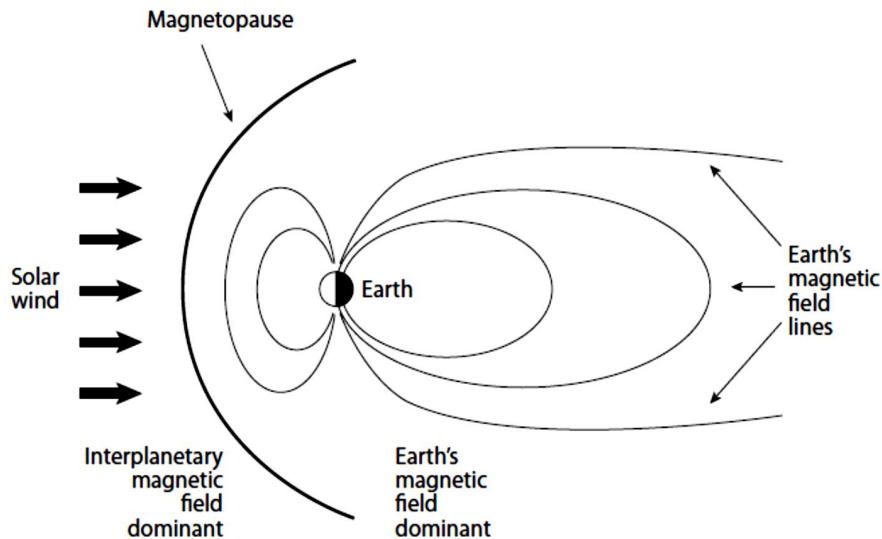


Figure 1.1: Earth's magnetosphere and solar wind sketch. Magnetic field lines are compressed in the dayside, while nightside magnetosphere is elongated in a tail-like structure of hundreds of Earth radii [2].

The Earth's magnetosphere is a highly dynamic structure that responds dramatically to solar variations. When the magnetosphere is sufficiently disturbed by the solar wind, there can be a significant loss of magnetospheric energy inside the ionosphere. In fact, ionosphere and magnetosphere constitute a system of different and interacting entities, whose coupling mechanism is not well understood yet. A deeper description about the physical processes taking place in these two interfacial regions follows in the next section.

## 1.2 Implications of Magnetosphere-Ionosphere Coupling

Magnetosphere and ionosphere form a closely-coupled system, since Earth's magnetic field connects these two regions electrically; the resulting interaction causes an exchange of energy and momentum between them.

As net result, when the magnetosphere-ionosphere system is not treated as a whole and it is not examined in its entirety, it is not possible to have a complete overview of high and low-altitude regions of Earth-space.

The reciprocal coupling between these interacting entities is identified in several processes which conjoin the lower-altitude ionospheric plasma with the energized plasmas of the high-altitude magnetosphere: their connection is responsible for space weather phenomena as magnetospheric substorms, ionospheric signatures, and the penetration of high-latitude electric field into low latitudes [3]. Between the previously mentioned space events, this study is concentrated within auroral signatures.

Common to all of these features, there is not a full understanding of magnetospheric generator mechanisms responsible for phenomena observed in the ionosphere.

The energy transfer from the magnetosphere to the ionosphere has been widely described by theoretical models; on the other hand, without adequate observations in the source region, no theories can be verified [4].

The absence of mapping magnetospheric measurements to the ionosphere prevents the knowledge of the energy extraction from the magnetosphere and the conditions and location of ionospheric phenomena.

The application that is analyzed for the magnetic field line mapping between the magnetosphere and ionosphere is the use of a satellite floating in the magnetosphere and emitting an electron beam.

### 1.2.1 Ionospheric Signatures

Auroras occur when there is a temporary disturbance of Earth's magnetosphere coming from the sun in the form of solar wind, high-energy particle clouds, or X-rays.

The initial disturbance from the sun exhibits as an increased plasma movement through the magnetosphere and an increased electric current in the ionosphere. In fact, most of the sun particles and radiation are deflected by the magnetosphere, but some of them are trapped.

Trapped charged particles are accelerated through the magnetic field toward the polar regions and they precipitate into the upper atmosphere.

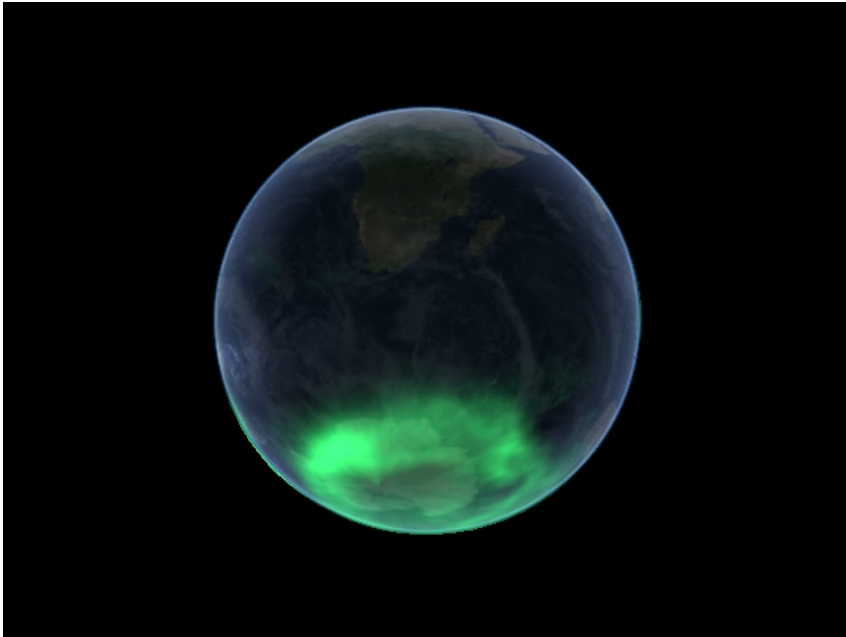


Figure 1.2: A view of the aurora australis taken by the Imager for Magnetopause-to-Aurora Global Exploration (IMAGE) spacecraft on January 2005. The auroral oval is visible [5].



Figure 1.3: Northern Lights over Alaska in the night of February 16, 2017, Poker Flat Research Range, Fairbanks [5].

In particular, streaming electrons and ions form ring-shaped areas centered around the magnetic poles of Earth, called auroral ovals (fig.1.2).

The diameter of an auroral oval diameter is approximately 3000 km, growing larger when the magnetosphere is more disturbed.

When particles strike the ionosphere, they collide with atmospheric constituents.

As fast-moving particles from the magnetosphere rain into the ionosphere, atmospheric gases receive energy and they move to an excited state. Molecules return to their normal state losing their energy by emission of photons.

If a considerable amount of collisions occur, the atmospheric elements emit light within the visible spectrum (fig.1.3). The color of the aurora depends on which gas is excited and on how much energy is exchanged [5].

The two main molecular constituents of the atmosphere comprise that of oxygen and nitrogen, which emit a green-orange/red light, and blue or red light respectively. The oxygen and nitrogen molecules also emit ultraviolet light, which can only be detected by special cameras on satellites. Green is the most common color.

About 30 % of the total energy of the magnetotail goes into Joule heating and precipitation heating of the auroral ionosphere.

On the other hand, since a coupled system is considered, auroras have a significant impact on the magnetosphere too. There is not still an unambiguous determination of the generator mechanisms that rule the ground signatures, so the returning impact of auroras on the magnetosphere is not known as well.

### 1.2.2 A possible solution for MI coupling understanding

The auroral ionosphere and nightside magnetosphere are connected through the time varying magnetic field. In order to study how auroras are powered by the magnetosphere, the measurements from the respective regions needs to be collected.

A versatile and possible solution to perform space measurements can be the use of a satellite flying at a geosynchronous orbit (the generator region of ionospheric signatures).

The first consideration is to determine if the satellite is *on* a magnetic field line that connect to the aurora in the ionosphere [6]. For this purpose, it is possible to mount an electron gun on the magnetospheric satellite: the electrons fired from the spacecraft travel along the magnetic field line, producing a detectable beam spot in the atmosphere. In other words, the electron beam illuminates the magnetic footpoint of the satellite in the upper atmosphere: it is used as a magnetic field line *tracer*, to connect magnetospheric phenomena with their image in the ionosphere.

One major difficulty of the electron gun approach is the spacecraft charging. As the electron beam is fired, the spacecraft charges and it can reach high levels of

potential that prevent the emission itself. In the worst case scenario, the spacecraft charging could be catastrophic for the mission success.

We devote the last section of this chapter to a qualitative description of spacecraft charging.

### 1.3 Spacecraft charging

Spacecraft charging occurs when charged particles from ambient plasma and the surrounding environment stop on the spacecraft [7]. A net positive or negative charge is accumulated on the satellite. Likewise, if the spacecraft potential relative to the surrounding plasma potential is different from zero, the spacecraft is charged.

Different classes of spacecraft charging can be distinguished.

When the spacecraft is made of a conductive material, charges lie on the surfaces (*surface charging* case). If the spacecraft is composed of electrically separated surfaces, they can be at different potentials. This is a *differential charging* situation. The spacecraft may be surrounded by a high-energy particle environment, and electrons and ions may penetrate dielectrics. This spacecraft charging is called *bulk charging*.

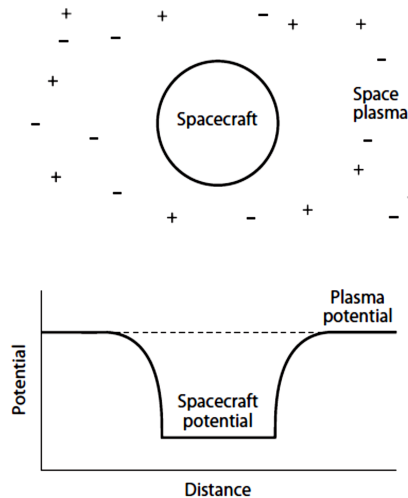


Figure 1.4: Potential of a charged spacecraft. Since the spacecraft potential differs from ambient potential, a sheath around it is formed. The plasma inside the sheath is nonneutral [2].

### 1.3.1 Cause and effects

Satellite charging levels are determined by current balance [2]: spacecraft can be considered as a node in a circuit in space, and, according to Kirchhoff's circuital laws, in equilibrium conditions all currents (incoming and outgoing) sum to zero. The current balance equation determines the potential at which equilibrium is achieved; in particular, the resulting potential is the potential difference between a spacecraft and the surrounding space plasma environment [7]. Equilibrium is typically reached in a few milliseconds. A spacecraft orbiting around Earth is subject to different currents:

- *background current*, carried by ions and electrons coming from background plasma;
- *secondary current*, due to charged particles hitting spacecraft's surface that might cause the emission of the so-called secondary electrons;
- *backscattering current*: when electrons from space impact the satellite and they are absorbed, they can experience a series of scattering inside the material; then these particles are emitted again;
- *photoelectric current*, given by exposure of material to photons coming from the sun (satellite emits electrons);
- *artificial current*, including electrons beams, ion thrusters, plasma contactors.

Some currents will charge the spacecraft positively, others will have the opposite effect.

At equilibrium, spacecraft will be in floating conditions<sup>1</sup>, and its charge will be nonzero. Spacecraft charging relies basically on the space region in which spacecraft is, material of its surface and space weather.

If electron or ion beams are emitted, the net beam currents leaving the probe have to be taken into account also; the higher the beam-induced potentials are, the more significant current flows are.

Usually, four separate locations are identified [2]:

1. *geosynchronous altitudes*

At geosynchronous altitudes, the spacecraft is in this low-density and high-energy plasma region, so high-level spacecraft charging may occur.

---

<sup>1</sup>A *floating* potential is the potential assumed by a probe when the net current collected by it is zero.

## 2. *Low Earth orbits*

These altitudes (few hundreds of kilometers) are characterized by a low-energy and high-density plasma; background can provide a sufficient current to neutralize a charged spacecraft. For this reason, Low Earth Orbit (LEO) satellite charging is not of considerable concern.

## 3. *Auroral latitudes*

At auroral latitudes (60° - 70° latitudes) high-energy electrons precipitations take place. The energy distribution of electrons in the excited state is equivalent to an electron beam energy distribution; when energetic particles precipitate at these latitudes, high-level surface charging arises.

## 4. *Radiation belts*

The Earth has two radiation belts, located at the inner region of magnetosphere. Radiation belts are highly energetic charged particles zones. They actually act like barriers that prevent electrons from reaching the Earth. The belts endanger satellites, because of the very high radiation. For this reason, deep dielectric charging is an important issue: fast particles penetrate nonconducting materials, and finally deposit their energy. Spacecrafts orbiting for a long time in this area must be projected with an adequate shielding, because internal damage may occur.

Orbit	Description	Altitudes
LEO	Low Earth orbit	200 – 2000 km
MEO	Medium Earth orbit	2000 – 35790 km
GEO	Geosynchronous orbit	35790 km
HEO	High Earth orbit	> 35790 km

Table 1.1: Altitude classification of various Earth orbits [8].

Low Earth orbit region is characterized by a high-density and low-energy plasma ( $n \sim 10^5 \text{ cm}^{-3}$ ,  $T \sim 0.1 \text{ eV}$ ); at geosynchronous orbit, space plasma has high energy (about 1 keV) and low density ( $< 1 \text{ cm}^{-3}$ ) [2].

Satellite charging is hazardous mainly for onboard electronics and scientific measurements on spacecraft itself [2].

Charging in a radioactive environment affects operations, navigation and survivability of the spacecraft. If the spacecraft is not accurately screened, there can

be disturbances that affect telemetry. When the spacecraft surfaces are at different potentials, electrical problems such as arcing or uncontrolled fast discharges between surfaces and the external space may occur. Electrical discharges are of serious concern as they cause interferences and malfunctioning in the electronic onboard instruments.

The interference with scientific measurements is related to the fact that a charged object repels one type of charge and attracts the other.

Around a charged spacecraft a sheath is created: the spacecraft is surrounded by a thin 'layer' in which ion and electron densities are not equal. The creation of a sheath inevitably affects the measurements of density, energy, electric fields and pitch angle (the angle between the vectors representing the local magnetic field and the velocity of a particle).

### 1.3.2 Mitigation

All orbiting spacecrafts accumulate electric charge from the surrounding natural space plasma.

Varied mitigation systems have been tested to reduce the impact of phenomena caused by spacecraft charging.

Mitigation methods can be primarily divided into two classes: active and passive.

Active methods need a power source and control commands. Passive methods activate and work automatically.

Alternatively, mitigation methods are divided in two additional groups, according to their operating principle: *injection* or *collection*. In the former case the removal of the charge accumulated on the satellite relies on the emission of charged particles away from the spacecraft. The collection technique consists of drawing a neutralizing current from the background environment to compensate for the excessive charge on the satellite.

Basic mitigation designs are presented in short.

- *Electron emission*

Electron emission is the most direct method to eliminate excess electrons from a conducting spacecraft. On the other hand, electron emission is not a suitable technique for dielectric surfaces, that are not conductive. In the latter case, differential charging occurs.

- *Ion emission*

Idealizing a highly negatively charged spacecraft, an ion emission may be effective in the elimination of net satellite charge.

If the beam energy is low, ions are attracted back toward the probe. If ion potential energy is higher than spacecraft potential, after their emission ions escape.

Satellite surface neutralization by returning ions may be attributed to two processes: returning ions deposit their positive charge and, at the same time, they generate secondary electrons that exit the spacecraft, leaving behind an additional positive charge [9]. This method is effective in mitigating differential charging.

The experimental satellite SCATHA (Spacecraft Charging AT High Altitude), launched in 1979, was one of the first research satellites designed to explore the effects of spacecraft charging at geosynchronous altitudes. In this orbit a spacecraft is usually negatively charged when it goes under eclipse. Electron and ion beam experiments have been conducted on SCATHA, revealing that the electron beam has been inefficient for discharging. Low energy ion beam succeeded in the complete removal of satellite excess charge.

- *Plasma emission*

An alternative concept for spacecraft charging mitigation is emitting particles of both species.

The accumulation of an excessive charge on the satellite may be prevented more efficiently with plasma ejection, which is more effective with respect to electron or ion emission alone.

The level of discharging depends on the beam current and energy, as well as ambient conditions. Ejection of electron and ion beams, or plasma emission can control the spacecraft potential, when the beam current exceeds the ambient current.

Mitigation technologies for spacecrafts emitting an electron beam will be examined in the next chapter.

# Chapter 2

## Theoretical model for the transient of a magnetospheric spacecraft emitting a high-power electron beam

In this chapter spacecraft charging issue is detailed, focusing on applications that include high-power electron beams. Different mitigation solutions are investigated in section 2.1. In section 2.2, a theoretical model aimed to simulate time evolution of the system based on the most suitable mitigation scheme is introduced.

### 2.1 Spacecraft charging mitigation scheme

#### 2.1.1 Spacecraft charging equation

The spacecraft charging equation is shown in order to prove that a beam emitted in either a vacuum or a low-density background returns to the spacecraft [10]. As explained in section 1.3.1, probe charge is subject to a transient that ends when the satellite reaches floating conditions.

The net charge on the spacecraft is indicated with  $Q_{sc}$ .

$$\frac{dQ_{sc}}{dt} = I_e^{bg} + I_i^{bg} + I_e^{sec} + I_e^{bs} + I_e^{ph} + I_e^a + I_i^a \quad (2.1)$$

- $(I_e^{bg} + I_i^{bg})$  is associated to electron and ion fluxes from background;
- $I_e^{sec}$  is secondary electron current;

- $I_e^{bc}$  is backscattering current;
- $I_e^{ph}$  indicates photoelectron current;
- $(I_e^a + I_i^a)$  represents artificial currents emitted by the spacecraft itself.

Secondary, backscattering, photoelectron currents are ignored from now on.

We start from the vacuum case.

If the spacecraft is approximated to a spherical conductor of radius  $R_{sc}$ , a capacitance  $C_{sc}$  is in turn introduced to express the spacecraft charge as a function of its potential  $\phi_{sc}$ . Capacitance of a conductive sphere of radius  $R_{sc}$  is defined as (where  $\epsilon_0$  is the vacuum permittivity):

$$C_{sc} = 4\pi\epsilon_0 R_{sc} \quad (2.2)$$

The net charge on the satellite is the product between potential and capacitance:

$$Q_{sc} = 4\pi\epsilon_0 R_{sc} \phi_{sc} \quad (2.3)$$

For a spacecraft emitting a beam in vacuum, with current  $I_e^b$ , equation (2.1) is reduced to :

$$4\pi\epsilon_0 R_{sc} \frac{d\phi_{sc}}{dt} = I_e^b \quad (2.4)$$

The attempt is to establish in which conditions the electron beam returns to the spacecraft, giving a numerical example. Electrons of the beam return when the satellite potential equals the kinetic energy of the beam:

$$e\phi_{sc}^{return} = \frac{1}{2}m_e v_b^2 \quad (2.5)$$

Quantities in the equation above are the elementary charge  $e$ , the electron mass  $m_e$ , and the beam velocity  $v_b$ .

From equations (2.4) and (2.5), assuming  $\phi_{sc} = 0$  at  $t_0 = 0$ , the time  $\tilde{t}$  required to the beam to be pulled back is:

$$\tilde{t} = 4\pi\epsilon_0 R_{sc} \frac{\phi_{sc}^{return}}{I_e^b} \quad (2.6)$$

For a 100 keV beam, with a current  $I_e^b = 10$  mA fired from a spacecraft whose radius  $R_{sc} = 1$  m,  $\tilde{t} \simeq 1.1$  ms.

We consider now the background plasma case.

The calculation of the spacecraft potential at equilibrium conditions is performed; the target is to derive the current needed to be carried by background plasma itself

to balance the electron beam. The equilibrium condition is set by imposing a null time derivative of  $Q_{sc}$  in the equation (2.1):

$$I_e^b + I_e^{bg} + I_i^{bg} = 0 \quad (2.7)$$

Background currents are estimated through Orbital-Motion-Limited (OML) theory [11], [12]; this expression is a function of background plasma parameters, and is valid when the probe potential is greater than zero. Magnetic fields effects are neglected in the OML theory.

$$I_e^{bg} = -e\sqrt{8\pi}R_{sc}^2n_e\sqrt{\frac{T_e}{m_e}}\left(1 + e\frac{\phi_{sc}}{T_e}\right) \quad (2.8a)$$

$$I_i^{bg} = e\sqrt{8\pi}R_{sc}^2n_i\sqrt{\frac{T_i}{m_i}}\exp\left(-e\frac{\phi_{sc}}{T_i}\right) \quad (2.8b)$$

Electron and ion background densities are identified with  $n_e$  and  $n_i$ , with  $T_e$  and  $T_i$  representing their temperatures. Typical values of density and temperature at geosynchronous orbit are  $n_e = n_i = 10^6 \text{ m}^{-3}$ ,  $T_e = T_i = 1 \text{ keV}$ .

Solving the equation numerically for a beam of current  $I_e^b = 10 \text{ mA}$ , the spacecraft should reach an equilibrium potential of about 1 MV to collect background electrons that can compensate the beam current [10]. On the other hand, the equilibrium potential is higher than  $\phi_{sc}^{return}$ , and the emitter would decelerate the beam, preventing its escape to infinity.

In conclusion, background plasma with typical geosynchronous orbit characteristics, cannot provide a returning current that is sufficient to offset high-power electron beams.

The background current may increase, as can be deduced from equation (2.8a), if spacecraft radius is bigger, or when the background electron density and temperature are higher.

Specifically, density dependence justifies the success of past missions and beam experiments in the ionosphere, where spacecraft can draw a substantial neutralizing current from the surrounding plasma medium [13], [14]. High background density prevents beam electrons to return, providing an appreciable current that impedes an excessive spacecraft charging.

### 2.1.2 Electron beam balanced by ion beam

The first strategy to mitigate spacecraft charging is to balance the electron beam with an ion beam of equal current.

To investigate the feasibility of ion beam emission, a simple system is considered,

consisting of the spacecraft, or the emitter, and the zero-potential background<sup>1</sup>, assuming a 1D planar geometry. The described system can be considered as a diode where charges are emitted from the satellite (*anode*) at  $\phi > 0$  and collected on a grounded surface (*cathode*), located at a certain distance  $d$ . An electric force moves ions toward the grounded surface, and an ion current is established.

Current that can be carried by ions is limited by space charge effects.

The notion of space charge is to look at discrete point-like particles as a continuum of charges enclosed in a finite volume region. Ions that are injected in the interelectrode volume create a space charge, proportionally to their current. If the current increases, a greater number of ions is injected in the system and the space charge rises. However, the space charge accumulated between the electrodes creates a potential distribution, inducing a repulsive force on the anode ions. As a consequence, the space charge may reduce the current that flows in the diode.

For the limit case of zero injection velocity [15], the maximum density current  $J_i^{max}$  that it is possible to carry has the following expression :

$$J_i^{max} = K \frac{\phi^{3/2}}{d^2} \quad (2.9)$$

$K$  is a constant  $\phi$  is the potential difference between anode and cathode;  $d$  is the distance separating the cathode and the anode.

Equation (2.9) is the well-known expression of Child-Langmuir's law [16],[17]; it states that the space charge limited current (SCLC) in a planar diode varies directly as the three-halves power of the potential difference and inversely as the square of the distance between electrodes.

If ions have a non-zero injection velocity [15], the potential distribution may be non-monotonic and present a maximum point  $\phi_{max}$  in front of the anode, known as *virtual anode*.

The virtual anode reflects back ions with a kinetic energy smaller than the potential difference ( $\phi_{max} - \phi$ ). As a result, only a fraction of the emitted current will reach the cathode.

Since the Child-Langmuir space charge limit lowers ion emission, it is not feasible to draw a large ion current with an ion beam.

Authors of [18] performed numerical simulations, proving that the maximum drawing current before space charge effects become dominant is lower than the current

---

<sup>1</sup>In the spacecraft charging community, the ambient space plasma potential is defined as zero. Actually, space plasma densities are subject to fluctuations, that are much faster than spacecraft potential variation, since plasma characteristic time scale is proportional to the inverse of plasma frequency [2].

needed to balance a high-power electron beam.

The ion beam scheme does not overcome the problem of spacecraft charging.

### 2.1.3 Plasma contactor

An alternative mitigation scheme to the ion beam is through plasma contactor technology.

A high-density plasma is fired from the spacecraft before beam activation and simultaneously with its emission.

A plasma contactor, made up of movable electrons and ions, creates a conductive path through which background plasma particles are collected, and ultimately neutralize the built up charge on the spacecraft.

In other words, contactor plasma takes on the role of a conducting bridge between ambient plasma and the satellite: it collects particles from the background (increasing the collection area surrounding the probe), and thus particles collected inside this high conductivity region, move toward the spacecraft.

Plasma contactor technology has been adopted to prevent spacecraft charging in different missions [19], [20], [21]. Nonetheless, in space active experiments with electron beams in the low-density magnetosphere, this mitigation scheme has yet to be tested.

Particle-In-Cell (PIC) simulations have been performed in [10] and [18], to investigate which conditions ensure the removal of residual positive charge left behind from the electron beam.

Numerical simulations results have shown that electron collection mode fails to draw a sufficient returning current from the background.

When contactor emission occurs only before the beam activation, contactor electrons are reabsorbed by the spacecraft, once the beam is turned on. At this point, the probe loses contact with contactor ions, that are pushed away; there is no more a plasma cloud that allows for the collection of ambient particles able to neutralize the satellite. The global effect is equivalent to a situation where contactor plasma is absent.

If contactor emission is maintained for the entire transient, with a contactor current  $I_c$  smaller than beam current  $I_b$ , background electrons may be accelerated through the contactor plume, but it would not be guaranteed that they are trapped inside the collection surface. In fact, the contactor cloud is collisionless and for this reason, it is transparent to background electrons [4].

The conclusion is that the plasma contactor cannot make contact between magnetospheric plasma and spacecraft.

However, in the case in which contactor plasma is kept on prior to and during beam emission, setting  $I_c > I_b$ , it may work as a net positive charge emitter.

After the beam firing and contactor electrons absorption, the spacecraft does not lose contact with ion cloud, that keeps expanding, reaching a size in which there are no space charge limits on ion emission. The crucial difference with respect to the electron collection route is that satellite potential no longer depends on the connection with the surrounding environment and background parameters, but rather it is controlled by the current emitted at the surface of contactor cloud.

Since contactor plasma enables a substantial ion current, this configuration is referred to as *ion emission* mode.

Numerical PIC simulations confirmed that the potential transient can be mitigated through ion emission configuration; actually PIC codes can be employed to represent just the early stage of a space experiment transient; later behavior of the system still needs to be reproduced and predicted.

Upon this basis, a mathematical model has been developed.

#### 2.1.4 CONNEX

CONNEX (CONNecTion EXplorer) is a mission currently under development, aimed to establish a connection between the magnetosphere and ionosphere, using an active mapping technique.

CONNEX is a multi-component system: the space segment is made up of a large satellite and four smaller satellites in constellation in the geosynchronous-orbit equator (see fig. 2.1); the ground component has a set of all-sky cameras, optical beam-spot locators and ionospheric radars [22].

The mother spacecraft has an electron accelerator that certifies the satellite-auroral conjugacy by marking magnetospheric footpoint in the ionosphere. The electron beam is fired with a pulse of 0.5 s. Its nominal power is 1 kW, the kinetic energy is 1 MeV and its current 1 mA. Alternatively, a 100 keV electron beam, carrying a current of 10 mA can be used. To prevent severe charge accumulation, the probe emits a plasma contactor. Daughter spacecrafts measure critical plasma gradients and fields in the magnetosphere.

The CONNEX mission presents different challenges in its architecture: spacecraft charging mitigation issues, validation of new relativistic electron accelerator technologies, and beam propagation, stability and detection [23].

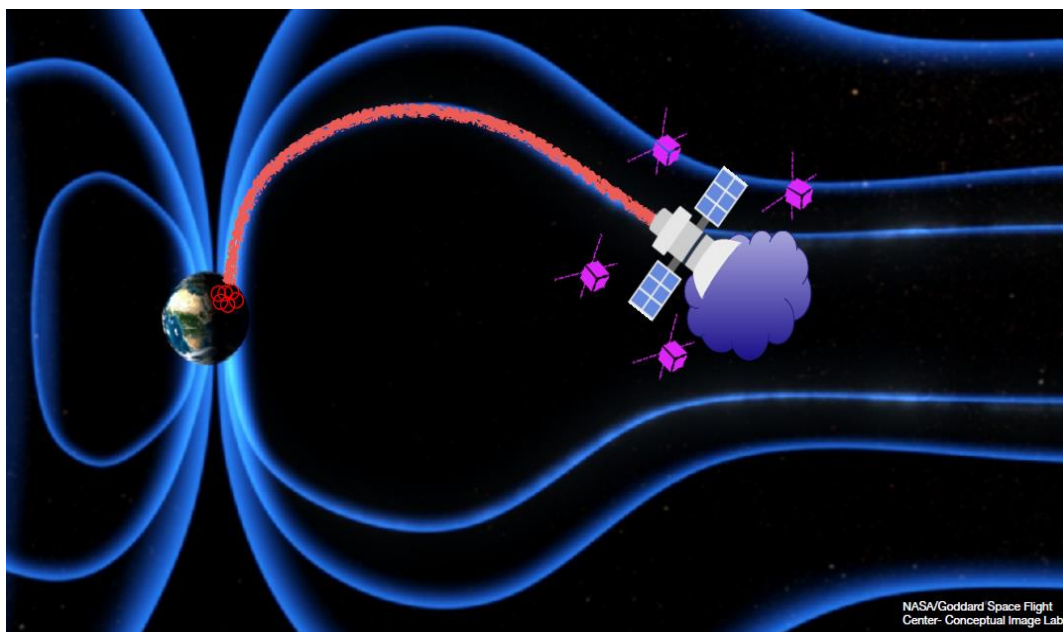


Figure 2.1: Sketch of CONNEX spacecrafts and spot of electron beam traveling along a magnetic field line [22].

## 2.2 Theoretical model

In this section, the spacecraft-charging mitigation scheme based on plasma contactor is analyzed.

The spacecraft charging process is separated into two phases: in the first stage, until  $\tau = \tau_c$ , the spacecraft emits only the contactor plasma (*contactor expansion regime*); for  $\tau \geq \tau_c$ , the electron beam is fired, while the contactor emission is preserved (*beam emission regime*).

During the transient, contactor electrons and ions leave the satellite with currents equal to  $I_e$  and  $I_i$ , respectively. When the beam is turned on, beam electrons move, resulting in the drawing of a current  $I_b$ .

Being that the fundamental process that determines the surface potential at equilibrium is the current balance [2], the emitter is regarded to be in floating conditions during both regimes. In particular, at the time of beam emission, neglecting non-artificial currents:

$$I_i = I_b + I_e \quad (2.10)$$

A semi-analytical model has been developed from authors of [24] to simulate the

transient of beam emission regime.

### 2.2.1 Basic assumptions

The studied system includes the spacecraft, the electron beam and the plasma contactor; it has a simple reference geometry: the spacecraft is represented as a sphere of radius  $r = R_{sc}$ , located in a finite domain, having an outer boundary that is a grounded sphere of radius  $r_2$ , concentric to the spacecraft.

The problem has spherical symmetry, and both emissions of electron beam and contactor plasma are assumed to be isotropic. The model is one-dimensional along the radial coordinate  $r$ .

Contactor electrons at the injection point have a Maxwellian-distributed velocity, while contactor ions are cold and are accelerated through a finite drift velocity directed radially. Electron thermal speed is greater than drift velocity, and, accounting for equal densities of electrons and ions at injection [10], [18], there are different currents at the emission point.

Once the beam is turned on, it leaves behind a positive charge equal to  $Q_b = I_b \cdot t$ . Consequently, spacecraft potential increases in time, affecting contactor cloud arrangement: contactor electrons are pulled back to the satellite, adapting their position to the charge accumulated on the emitter itself. At this point, two areas of the contactor cloud can be distinguished: a *quasi-neutral region*, from the spacecraft position to  $r_{qn}$ , and an ion region, that starts at point  $r_{qn}$  until  $r_i$ . In the first region, electron and ion densities balance each other  $n_i \approx n_e$ , while in the ion region plasma is non-neutral ( $n_i > n_e$ ).

The quasi-neutral cloud is supposed to enclose a net charge equal to zero. Even if in this zone the total charge is not exactly null, it is still negligible with respect to the overall charge of the system,  $Q_{tot} \approx 0$ . Since the quasi-neutral region is considered to be neutral, the positive charge  $Q_b$  is transferred instantaneously to the ion region.

The model allows for no potential drop across quasi-neutral cloud:  $\phi(R_{sc}) = \phi(r_{qn})$ .

It is assumed that beyond the ion region there is vacuum ( $r \geq r_i$ ).

The plasma plume and the background plasma densities are very different, the physics of the plume expansion is described well enough by studying its expansion in vacuum [25].

This hypothesis is conservative, since [10] has been proven that a low-density background plasma slightly attenuates spacecraft charging.

Two other assumptions that are consistent with the previous one are taken into account: the electron beam velocity is infinite; beam current equals ion contactor current.

The latter supposition implies the neglect of fast electrons transient; their dynamics is not studied and the electron contactor current approaches rapidly to zero as the beam is turned on ( $I_e \rightarrow 0$ ). Equation (2.10) is simplified to  $I_i = I_b$ .

The characteristic time scale of ions is longer than the corresponding electrons; it is assumed that system evolution is driven by ion dynamics and the electrons are assumed to be in equilibrium.

Time evolution is studied with a quasi-static approximation; a snapshots of static state sequences, and instantaneous quantities are calculated at each step, solving equations that are valid in steady state.

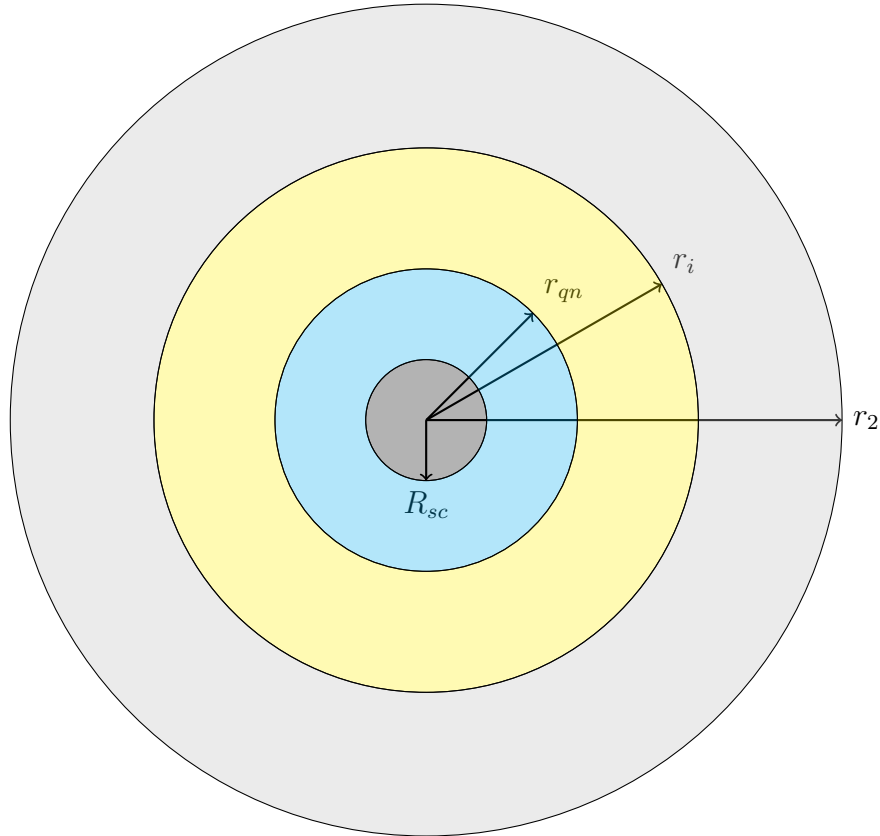


Figure 2.2: Reference geometry of semy-analytical model: spacecraft (*dark grey*), quasi-neutral region (*cyan*), ion region (*yellow*), vacuum (*gray*).

### 2.2.2 Normalization

Characteristics or properties of a system are expressed very often through dimensionless parameters, such that any change in scale does not affect the magnitude of these quantities.

To obtain normalized variables, we need to specify reference quantities.

Reference density  $n_{ref}$  temperature  $T_{ref}$  are defined, because through them two important parameters in plasma physics can be determined: Debye length and electron plasma frequency.

Normalization procedure that was followed for single variables is summarized in table 2.1.

Quantity	Reference quantity	Normalization
Temperature $T$	$T_{ref}$	$\hat{T} = T/T_{ref}$
Density $n$	$n_{ref}$	$\hat{n} = n/n_{ref}$
Length $r$	$\lambda_{ref} = \sqrt{\frac{K_B T_{ref}}{n_{ref} e^2} \epsilon_0}$	$\hat{r} = r/\lambda_{ref}$
Velocity $v$	$v_{ref} = \sqrt{\frac{K_B T_{ref}}{m_e}}$	$\hat{v} = v/v_{ref}$
Time $t$	$\omega_{ref} = \sqrt{\frac{n_{ref} e^2}{m_e \epsilon_0}}$	$\tau = t \cdot \omega_{ref}$
Electrostatic potential $\phi$	$\phi_{ref} = \frac{K_B T_{ref}}{e}$	$\psi = \phi/\phi_{ref}$
Current $I$	$I_{ref} = e \cdot n_{ref} v_{ref} \lambda_{ref}^2$	$\hat{I} = I/I_{ref}$
Charge $Q$	$Q_{ref} = e \cdot n_{ref} \lambda_{ref}^3$	$\hat{Q} = Q/Q_{ref}$

Table 2.1: Normalized variables

To normalize an entire equation, all the variables that appear in it have to be normalized.

An example by means of the equation of motion is given considering the case of a particle with charge  $q$ , moved by an electric force  $q \cdot E$  in a generic one-dimensional geometry.

$$\begin{cases} \frac{dr}{dt} = v \\ \frac{dv}{dt} = \frac{q}{m} E \end{cases} \quad (2.11)$$

We set the following equalities:

$$\begin{aligned}
 v &= \hat{v} \cdot v_{ref} \\
 t &= \tau / \omega_{ref} \\
 E &= \hat{E} \cdot E_{ref}
 \end{aligned} \tag{2.12}$$

The reference electric field is simply the ratio between the reference potential and the Debye length:  $E_{ref} = \phi_{ref} / \lambda_{ref}$ .

The second equation of the system (2.11) can be rewritten as follows:

$$\frac{d\hat{v}}{d\tau} \cdot v_{ref} \cdot \omega_{ref} = \frac{q}{m} \hat{E} \cdot E_{ref} \tag{2.13a}$$

$$\frac{d\hat{v}}{d\tau} = \frac{q}{m} \hat{E} \frac{\phi_{ref}}{\lambda_{ref} v_{ref} \omega_{ref}} \tag{2.13b}$$

The right hand side of the previous expression can be simplified:

$$\frac{\phi_{ref}}{\lambda_{ref} v_{ref} \omega_{ref}} = \frac{K_B T_{ref}}{e} \cdot \left( \sqrt{\frac{K_B T_{ref}}{n_{ref} e^2}} \varepsilon_0 \cdot \sqrt{\frac{K_B T_{ref}}{m_e}} \cdot \sqrt{\frac{n_{ref} e^2}{m_e \varepsilon_0}} \right)^{-1} = \frac{m_e}{e} \tag{2.14}$$

So, calling  $\hat{q} = q/e$  and  $\hat{m} = m/m_e$ , the normalized equation of motion will be:

$$\frac{d\hat{v}}{d\tau} = \frac{\hat{q}}{\hat{m}} \hat{E} \tag{2.15}$$

### 2.2.3 Model equations

The four unknowns of the theoretical model are: radius of quasi-neutral cloud  $r_{qn}$ , ion front position  $r_i$ , ion front potential  $\phi_i$  and spacecraft potential  $\phi_{sc}$ ; they are derived from the equations we present below.

The non-dimensional quantities and the obtained equations are valid for the normalization summarized in table 2.1.

The parameter  $\hat{r}_{qn}$  can be properly described through a model that includes electron dynamics. However, assuming  $\hat{I}_b = \hat{I}_i$ , in the moment the beam starts to be fired, contactor electrons move toward the emitter very quickly with respect to the ion characteristic time scale; they readjust in response to the satellite potential in a time span during which ions have not moved considerably. After electron rearrangement, that can be thought as instantaneous, the electron contactor cloud does not vary

over time. The quasi-neutral coordinate is assumed to be equivalent to value of  $\hat{r}_{qn}$  at the beginning of beam emission regime. The relation used is in line with results shown in [18]:

$$\hat{r}_{qn}(\tau) = \hat{r}_{qn,0} \quad (2.16)$$

The equation of motion for ions is used to calculate the ion front position  $r_i$ :

$$\frac{d^2\hat{r}_i}{d\tau^2} = \frac{\hat{q}_i}{\hat{m}_i} \hat{E}(\hat{r}_i) \quad (2.17)$$

The electric field at the ion front position is obtained from Gauss's law

$$\hat{E}(\hat{r}_i) = \frac{\hat{Q}(\hat{r}_i)}{4\pi\hat{r}_i^2} \quad (2.18a)$$

It is noticed that the ion front is crossed only by the beam current, since contactor electrons are reabsorbed by the spacecraft. Calling  $\hat{Q}_{i,0}$  the charge inside the sphere of radius  $\hat{r}_i$  at  $\tau = \tau_c$ , charge  $\hat{Q}$  is:

$$\hat{Q} = \hat{Q}_{i,0} + \hat{I}_b\tau \quad (2.18b)$$

The final expression of ion equation of motion is written with its initial conditions:

$$\left\{ \begin{array}{l} \frac{d^2\hat{r}_i}{d\tau^2} = \frac{\hat{q}_i}{\hat{m}_i} \frac{\hat{Q}_{i,0} + \hat{I}_b\tau}{4\pi\hat{r}_i^2} \\ \hat{r}_i(\tau_c) = \hat{r}_{i,0} \\ \left. \frac{d\hat{r}_i}{d\tau} \right|_{\tau=\tau_c} = \hat{v}_{i,0} \end{array} \right. \quad (2.19)$$

It is indicated that  $\hat{r}_{i,0}$  and  $\hat{v}_{i,0}$  are position and velocity of the ion front at  $\tau = \tau_c$  respectively.

The equation to obtain the electrostatic potential at the ion front  $\psi_i$  is the Poisson's equation in vacuum. In the domain  $\hat{r} \in [\hat{r}_i, \hat{r}_2]$ , we have:

$$\left\{ \begin{array}{l} \frac{1}{\hat{r}^2} \frac{d}{d\hat{r}} \left( \hat{r}^2 \frac{d\psi}{d\hat{r}} \right) = 0 \\ \psi(\hat{r}_2) = 0 \\ \left. \frac{d\psi}{d\hat{r}} \right|_{\hat{r}=\hat{r}_i} = -\frac{\hat{Q}_{i,0} + \hat{I}_b \tau}{4\pi \hat{r}_i^2} \end{array} \right. \quad (2.20)$$

Solving the system above, the final expression of the ion front potential is the following:

$$\psi_i = \frac{\hat{Q}_{i,0} + \hat{I}_b \tau}{4\pi} \frac{\hat{r}_2 - \hat{r}_i}{\hat{r}_2 \hat{r}_i} \quad (2.21)$$

Alternatively, an equivalent vacuum capacitance  $\mathcal{C}$  such that  $\psi_i = \hat{Q}/\mathcal{C}$  can be introduced:

$$\mathcal{C} = 4\pi \frac{\hat{r}_2 \hat{r}_i}{\hat{r}_2 - \hat{r}_i} \quad (2.22)$$

The final equation that is needed for the spacecraft potential value is the Poisson's equation in the ion region ( $\hat{r} \in [\hat{r}_{qn}, \hat{r}_i]$ ). In fact, satellite potential is controlled by current that flows between the quasi-neutral cloud and the ion front.

$$\left\{ \begin{array}{l} \frac{1}{\hat{r}^2} \frac{d}{d\hat{r}} \left( \hat{r}^2 \frac{d\psi}{d\hat{r}} \right) = \hat{n}_e - \hat{n}_i \\ \psi(\hat{r}_i) = \psi_i \\ \left. \frac{d\psi}{d\hat{r}} \right|_{\hat{r}=\hat{r}_{qn}} = 0 \end{array} \right. \quad (2.23)$$

Densities appearing in the Poisson equation have steady-state expressions. Ions are considered cold and they enter the system with a drift velocity  $\hat{v}_d$ ; ion density  $\hat{n}_i$  is derived from continuity and momentum equations in steady-state:

$$\hat{n}_i = \frac{\hat{I}_b}{4\pi \hat{v}_d \hat{r}^2} \left( 1 + \frac{\psi_{sc} - \psi}{\frac{\hat{m}_i \hat{v}_d^2}{2}} \right)^{-1/2} \quad (2.24)$$

In the model, electrons have a Maxwellian distribution at the quasi-neutral surface and their density is expressed through Orbital-Motion-Limited approximation [12].

$$\hat{n}_e = \sqrt{\frac{\pi}{2}} \frac{\hat{J}_e}{\exp\left(\frac{\psi - \psi_{sc}}{\hat{T}_e}\right)} \left[ 1 + \operatorname{erf} \sqrt{\frac{\psi}{\hat{T}_e} - \frac{2}{\sqrt{\pi}}} \sqrt{\frac{\psi}{\hat{T}_e}} \exp\left(-\frac{\psi}{\hat{T}_e}\right) - \frac{\sqrt{z^2 - 1}}{z} \exp\left(\frac{\psi - \psi_{sc}}{\hat{T}_e(z^2 - 1)}\right) \right] \quad (2.25a)$$

if  $\psi(z) \leq \psi_{sc}/z^2$

$$\hat{n}_e = \sqrt{\frac{\pi}{2}} \frac{\hat{J}_e}{\exp\left(\frac{\psi - \psi_{sc}}{\hat{T}_e}\right)} \left[ 1 + \operatorname{erf} \sqrt{\frac{\psi}{\hat{T}_e} + \frac{2}{\sqrt{\pi}}} \left( \sqrt{\frac{1}{\hat{T}_e} \left( \psi - \frac{\psi_{sc}}{z^2} \right)} - \sqrt{\frac{\psi}{\hat{T}_e}} \right) \exp\left(-\frac{\psi}{\hat{T}_e}\right) - \frac{\sqrt{z^2 - 1}}{z} \exp\left(\frac{\psi - \psi_{sc}}{\hat{T}_e(z^2 - 1)}\right) \left( 1 + \operatorname{erf} \sqrt{\frac{1}{\hat{T}_e} \frac{z^2 \psi - \psi_{sc}}{z^2 - 1}} \right) \right] \quad (2.25b)$$

if  $\psi(z) \geq \psi_{sc}/z^2$

The second boundary condition of the Poisson equation derives from the assumption of net charge inside the quasi-neutral cloud, set to be zero. Therefore, the electric field in the quasi-neutral region is null. Finally, from the differential equation (2.23)  $\psi_{qn} = \psi(\hat{r}_{qn})$  is obtained, whose value is equivalent to the spacecraft potential, for the previous hypothesis of no potential drop across the quasi-neutral region.

In summary, the fundamental equations upon which the model is based are:

1. quasi-neutral position expression (2.16);
2. ion equation of motion (2.19);
3. Poisson equation in vacuum (2.20);
4. Poisson equation in the ion region (2.23).

To solve all the equations above, we need their initial conditions:  $\hat{r}_{qn,0}$ ,  $\hat{r}_{i,0}$ ,  $\hat{v}_{i,0}$  and  $\hat{Q}_{i,0}$ . The subscript '0' refers to the onset of electron beam. These quantities depend on contactor expansion evolution, prior to beam emission.

In particular they correspond to values calculated at the end of expansion  $\tau = \tau_c$ . A model for contactor expansion regime is needed; thanks to the latter complementary model, the entire transient would be fully described. In addition, spacecraft potential behavior for different input conditions can be predicted. A model for contactor expansion is proposed in chapter 3.



# Chapter 3

## Shell model for expansion of contactor plasma

In this chapter, the model developed by means of the so called *shell method* is presented. This model is used to study the transient of plasma contactor expansion before the electron beam emission. After giving some general concepts of the method in section 3.1, we apply it in the case of interest (section 3.3) and its results are compared to PIC outcomes (section 3.5). In section 3.6, the implemented shell code is utilized to obtain a scaling law for the spacecraft potential.

### 3.1 Algorithm

The shell method is a particle-based, gridless technique, suitable for problems involving symmetries in Vlasov-Poisson systems [26].

The advantage of using a gridless particle technique can be appreciated mainly in dealing with problems in which the physical domain filled by particles varies rapidly in time (e.g. plasma expansions and explosions).

The shell method algorithm employs a set of computational particles, that behave like spherical shells, upon which electric charge is distributed uniformly; for this reason, the method is used for *spherical symmetry* cases.

The generic formulation of the shell method starts initializing the phase-space coordinates  $\mathbf{x}$  and  $\mathbf{v}$ , for each of the  $N$  computational particles used during the simulation. Particles are then sorted according to their radial coordinate  $R_i = |\mathbf{x}_i|$ , with  $R_i > R_j$  if  $i > j$ .

Taking into account the spherical symmetry of the system, the electric field  $\mathbf{E}_i$  is purely radial and depends on the total charge located at  $R \leq R_i$ .

It can be computed through Gauss law:

$$\mathbf{E}_i = \frac{1}{4\pi\epsilon_0} \left( \sum_{j=1}^{i-1} q_j + \frac{1}{2}q_i \right) \frac{\mathbf{x}_i}{R_i^3} \quad (3.1)$$

In the equation (3.1):

- $\sum_{j=1}^{i-1} q_j$  is the total charge of particles located inside the sphere of radius  $R_i$
- $\frac{1}{2}q_i$  is a correction factor that provides the correct value of the field if a linear behaviour of  $\mathbf{E}$  is assumed. It can be explained considering that [26] for  $R = R_i - \varepsilon$  ( $\varepsilon > 0, \varepsilon \rightarrow 0^+$ ) and  $R = R_i + \varepsilon$ , total charge is respectively  $\sum_{j=1}^{i-1} q_j$  and  $\sum_{j=1}^i q_j$ .

The basic hypotheses through which we calculate the electric field exclude point-like particle interactions, seen that physical charges are represented by spherical shells whose charge is distributed *along* a surface. Thus, plasma collisionality is reduced [27] as the number of shells increases, and vanishes with  $N \rightarrow \infty$ .

Hence, the shell algorithm is appropriate for systems dominated by collective interactions (*electrostatic, collisionless plasmas*).

Since particles move under the action of a self-consistent electric field, ion and electron dynamics are simply described by equations of motion:

$$\begin{cases} \frac{d\mathbf{x}_i}{dt} = \mathbf{v}_i \\ \frac{d\mathbf{v}_i}{dt} = \frac{q_i}{m_i} \mathbf{E}_i \end{cases} \quad i=1,2,\dots,N \quad (3.2)$$

Equations (3.2) after having calculated  $\mathbf{E}$  for each  $R_i$  can be solved by using a suitable numerical method and choosing a time step smaller than the inverse of plasma frequency  $\omega_p$ .

## 3.2 A simpler formulation of the method

As anticipated in section 3.1, the electric field depends on distance  $R$  only, so the force law is spherically symmetric, and the angular momentum  $\mathbf{L} = \mathbf{x} \times (m\mathbf{v})$  is conserved.

In particular, the direction of the angular momentum vector, always perpendicular to the plane defined by  $\mathbf{x}$  and  $m\mathbf{v}$ , does not change, and the motion of particles will be confined on that fixed plane [28]. This problem can be further reduced to a 2D description.

After having generated the initial 3D coordinates for space  $\mathbf{x} = (x, y, z)$  and velocity  $\mathbf{v} = (v_x, v_y, v_z)$ , a set of 2D coordinates are introduced as follows:

$$\mathbf{X} = (R, 0) \tag{3.3a}$$

$$\mathbf{V} = (v_R, v_\perp) \tag{3.3b}$$

where:

$$R = |\mathbf{x}|$$

$$v_R = \mathbf{v} \cdot \hat{\mathbf{e}}_R = \mathbf{v} \cdot \frac{\mathbf{x}}{R} \tag{3.4}$$

$$v_\perp = \sqrt{|\mathbf{v}|^2 - v_R^2}$$

Particles are sorted according to their radial position  $r_i = |\mathbf{X}_i|$ .

## 3.3 Shell method for contactor expansion simulation

The shell method is now adopted to simulate the transient of contactor plasma expansion, before electron beam ignition.

This application of the shell method is aimed to provide initial conditions of the system related to the model discussed in chapter 2. For this reason, the shell model is built starting from hypotheses provided by authors of the work [24], that have been summarized in section 2.2 .

The implemented code has been written in MATLAB and FORTRAN.

### 3.3.1 Initial distribution

It is considered that the spacecraft is a perfectly spherical plasma source of radius  $R_{sc}$ ; at each time step, contactor plasma is emitted in vacuum at a distance  $r = R_{sc}$ ,

isotropically from the surface, with a radial drift velocity  $v_{drift}$ .

Since  $v_{th,e} \gg v_d$ , it can be assumed that electrons are ejected according to the half-width Maxwellian distribution at rest, while ions motion is basically driven by drift velocity.

At time  $t \rightarrow 0^-$ , the spacecraft is neutral, so its total charge is zero.

At  $t = 0$ , there is the first emission; ejected particles, located on the surface, are characterized by an initial velocity and charge.

As discussed in section 3.2, dealing with a central force system, evolution of particles depends on their radial coordinate only, although the initialization of phase space coordinates provides 3D vectors of position and velocity.

Regarding the hypotheses made on velocity, we point out that initial conditions of particle distribution function  $f(\mathbf{v})$  determine and affect the entire transient of the system [29].

It is assumed that the distribution function  $f(\mathbf{v})$  is the product of three independent normally distributed velocity variables, with a variance  $\sigma^2 = (K_B T)/m = v_{th}^2$  and a mean value  $\mu = 0$ .

$$f(\mathbf{v}) = f(v_x) \cdot f(v_y) \cdot f(v_z) \quad (3.5)$$

For each component of the velocity vector  $v_k$  ( $k = x, y, z$ ), the Maxwell-Boltzmann distribution is:

$$f(v_k) = \sqrt{\frac{m}{2\pi K_B T}} e^{-\frac{m v_k^2}{2K_B T}} \quad (3.6)$$

Switching to a 2D coordinated system equation (3.3b), there is a straightforward distinction between radial and tangent coordinates.

In Particle Simulations, a charge injection from a boundary into the system is reproduced using the *flux* of a distribution. The boundary can represent a physical interface or a computational case, as the spatial grid used in a PIC simulations.

The direction of the flux at the surface is established by the normal to the emitting surface itself.

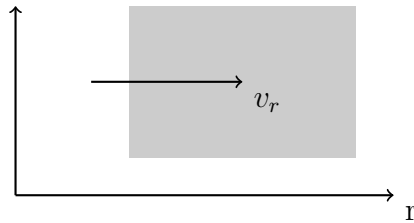


Figure 3.1: Example of a particle entering from the left boundary of a rectangular spatial grid with velocity  $v_r$ .

The velocity of particles coming from a Maxwellian source and entering the system was determined, starting from:

- Maxwellian flux with no drift for electrons;
- Maxwellian flux with a finite drift for ions.

The cumulative distribution function maps the flux of a distribution to uniformly distributed numbers  $\xi$ , between 0 and 1 [29].

For electrons and ions we can set respectively:

$$\xi = F(v_e) = \frac{\int_0^{v_e} v'_e e^{-v'^2_e / 2v_{th,e}^2} dv'_e}{\int_0^\infty v'_e e^{-v'^2_e / 2v_{th,e}^2} dv'_e} \quad (3.7)$$

$$\xi = F(v_i) = \frac{\int_0^{v_i} v'_i e^{-(v'_i - v_d)^2 / 2v_{th,i}^2} dv'_i}{\int_0^\infty v'_i e^{-(v'_i - v_d)^2 / 2v_{th,i}^2} dv'_i} \quad (3.8)$$

Both expressions can be inverted to obtain the injection velocities. For electrons:

$$v_e = v_{th,e} \sqrt{-2 (\log(1 - \xi))} \quad (3.9)$$

In the case of a Maxwellian flux with a drift, velocity cannot be written in a closed form, the equation can be inverted numerically.

On the other hand, if the drift is larger than the thermal velocity, the cumulative function of the flux can be approximated to that one of the *distribution* [29]:

$$\xi = F(v_i) = \frac{\int_0^{v_i} e^{-(v'_i - v_d)^2 / 2v_{th,i}^2} dv'_i}{\int_0^\infty e^{-(v'_i - v_d)^2 / 2v_{th,i}^2} dv'_i} \quad (3.10)$$

Whenever the drift velocity has not a relativistic component, it is added linearly to  $v$  ( $v''_i = v'_i - v_d$ ). From the latter equation, the ion velocity expression is deduced:

$$v_i = v_d + \sqrt{2} v_{th,i} \operatorname{erf}^{-1} \left( \xi + (1 - \xi) \operatorname{erf} \left( -\frac{v_d}{\sqrt{2}v_{th,i}} \right) \right) \quad (3.11)$$

Thus, it is emphasised that in the other directions, initial velocities are obtained from distribution and not from flux definition: the Maxwellian velocity can

be derived through equation (3.11), or, alternatively, recurring to the generation of normally distributed pseudorandom numbers.

To compute particle charge, an arbitrary number of shells shot at each time step  $dt$  needs to be chosen.

The single computational particle charge  $q_s$  is derived from the ratio between total charge emitted in a shot, proportional to input current,  $dQ_s$  and  $\Delta N_s$  ( $s = e$  for electrons,  $s = i$  for ions):

$$Q_s = I_s dt \tag{3.12a}$$

$$q_s = dQ_s / \Delta N_s \tag{3.12b}$$

Hence, at the first injection, the total charge left on the spacecraft is  $Q_{sc}(t_0) = -dQ_i + |dQ_e|$ .

### 3.3.2 Time evolution

At each time step  $dt$ ,  $\Delta N_e$  electrons and  $\Delta N_i$  ions are fired in vacuum: number of particles in the system increases and therefore the net charge on the spacecraft changes during the transient.

After the emission, charge motion is affected by the self-consistent electric field. It can happen that a particle reaches the satellite during its motion; hence, it has to be removed from the simulation, taking into account that its charge is accumulated onto the spacecraft surface.

Generally, the spacecraft charges negatively when an electron collides with it and it is absorbed.

Whenever an ion approaches to the surface, one or more electrons are stripped from the surface itself, to form a neutral atom. The global effect is that the satellite loses a number of electrons equal to the net charge of positive ion, and charges positively.

In the case of concern, the contactor currents are different at injection; in particular  $I_e > I_i$ . At the beginning of the transient, a net positive charge progressively accumulates on the spacecraft, and ions never reach its surface again. For what concerns electrons, fast negative particles of the system escape swiftly, while less energetic electrons are attracted back toward the satellite and some of them are absorbed.

Particles hitting the space probe can be identified by their radius  $r \leq R_{sc}$ . The final expression for the charge accumulated on the spacecraft, assumed to be a conductor, includes the correction of returning electrons.

At a generic time instant  $t$ :

$$Q_{sc}(t) = Q_{sc}(t - dt) - dQ_i + |dQ_e| - \left| \sum q_e \right|_{r \leq R_{sc}} \quad (3.13)$$

Whenever the emitter net charge is non-zero, the emitter itself creates a sheath that turns some of the emitted particles back, and in its neighborhood  $Q_{tot} \approx 0$  (see section 2.2.1).

Furthermore, a positive spacecraft potential forms a sheath that is shielded by recaptured electrons, after they readjust the current to  $I_e \sim I_i$  [18].

A quasi-neutral region is created as electrons move back toward spacecraft; it extends from spacecraft to position  $r_{qn}$ ; beyond this region, ions acquire a well-defined front (*ion region*). Finally, electrons that move ahead of the ions because of their greater thermal velocity, form a pure electron cloud beyond the ion region [30].

Additional functions for the calculation of potential and density are implemented, in such a way all the variables that are needed for the beam emission regime model can be defined.

### 3.3.3 Electric field

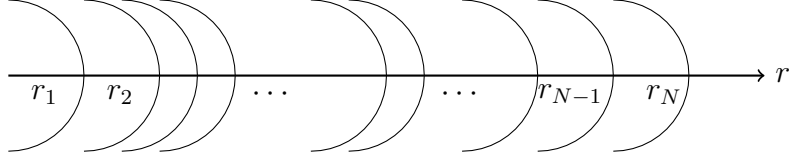
The expression of  $\mathbf{E}$  is obtained from the definition of the electric field generated by uniformly charged shells; in this case, the most internal shell coincides with the spacecraft charge, that affects the total charge of the system. The electric field equation, according to the simpler formulation explained in 3.2, is as follows:

$$\mathbf{E}_i = \frac{1}{4\pi\epsilon_0} \left( Q_{sc} + \sum_{j=1}^{i-1} \left( q_j + \frac{1}{2}q_i \right) \right) \frac{\mathbf{X}_i}{r_i^3} \quad (3.14)$$

### 3.3.4 Potential

The potential of the system is computed following two different approaches. The first procedure is based on two observations:

1. total charge of all shells sums to zero;
2. potential  $\phi(r) = \frac{1}{4\pi\epsilon_0} \frac{Q(r)}{r} + C$  is defined below a constant, and a reference point at zero potential has to be established.


 Figure 3.2: Shells sorted according to  $r$  in increasing order.

Considering  $N$  computational particles, already sorted in increasing order, at distances greater than the last particle position,  $r \geq r_N$ , total charge is zero and we set the potential to be null. The constant  $C$  is chosen to be zero for  $r \geq r_N$ . Taking two generic subintervals  $M$  and  $M + 1$  of  $r$  bounded by points  $r_{i-1}$ ,  $r_i$ ,  $r_{i+1}$ , the expressions of the potential can be written:

$$\phi(r)_M = \frac{Q_{i-1}}{4\pi\epsilon_0 r} + C_{i-1} \quad \text{if } r \in [r_{i-1}; r_i]$$

$$\phi(r)_{M+1} = \frac{Q_i}{4\pi\epsilon_0 r} + C_i \quad \text{if } r \in [r_i; r_{i+1}]$$

The charges  $Q_{i-1} = \sum_{j=1}^{i-1} q_j$  and  $Q_i = \sum_{j=1}^i q_j$  are the total charge enclosed by the sphere of radius  $r_{i-1}$  and  $r_i$  respectively.

At point  $r = r_i$  the potential has to be continuous, so we set:

$$\frac{Q_{i-1}}{4\pi\epsilon_0 r_i} + C_{i-1} = \frac{Q_i}{4\pi\epsilon_0 r_i} + C_i \quad (3.15a)$$

$$C_{i-1} = C_i + \frac{Q_i}{4\pi\epsilon_0 r_i} - \frac{Q_{i-1}}{4\pi\epsilon_0 r_i} = C_i + \frac{q_i}{4\pi\epsilon_0 r_i} \quad (3.15b)$$

Knowing that  $C_\infty = C_N = 0$ ,

$$\begin{aligned} C_{N-1} &= \frac{q_N}{4\pi\epsilon_0 r_N} \\ C_{N-2} &= \frac{q_{N-1}}{4\pi\epsilon_0 r_{N-1}} + C_{N-1} = \frac{q_{N-1}}{4\pi\epsilon_0 r_{N-1}} + \frac{q_N}{4\pi\epsilon_0 r_N} \\ &\vdots \\ C_2 &= \frac{1}{4\pi\epsilon_0} \left( \frac{q_3}{r_3} + \dots + \frac{q_{N-1}}{r_{N-1}} + \frac{q_N}{r_N} \right) \\ C_1 &= \frac{1}{4\pi\epsilon_0} \left( \frac{q_2}{r_2} + \frac{q_3}{r_3} + \dots + \frac{q_{N-1}}{r_{N-1}} + \frac{q_N}{r_N} \right) \end{aligned}$$

Finally, we compute the potential as a function of  $r$ :

$$\begin{cases} \phi(r_i) = \frac{1}{4\pi\epsilon_0} \left( \frac{Q_i}{r_i} + \sum_{j=i+1}^N \frac{q_j}{r_j} \right) & i = 1, 2, \dots, (N-1) \\ \phi(r_N) = 0 \end{cases} \quad (3.16)$$

The second approach is not derived by the total charge conservation, but rather implies the potential calculation through Gauss law. Knowing that  $E(r) = -d\phi(r)/dr$ , the potential difference between two successive radial coordinates is:

$$\phi_{i+1} - \phi_i = -\frac{1}{4\pi\epsilon_0} \int_{r_i}^{r_{i+1}} \frac{Q_i}{r^2} dr = \frac{Q_i}{4\pi\epsilon_0} \left( \frac{1}{r_{i+1}} - \frac{1}{r_i} \right) \quad (3.17)$$

It is indicated once again that the cumulative charge inside the sphere of radius  $r \leq r_i$  through the quantity  $Q_i$ .

At the last charge position, the potential is  $\phi_N = Q_N/r_N$ . The potential value at different points  $r_i$  can be evaluated as:

$$\phi_N - \phi_{N-1} = \frac{Q_{N-1}}{4\pi\epsilon_0} \left( \frac{1}{r_N} - \frac{1}{r_{N-1}} \right) \quad (3.18a)$$

$$\phi_{N-1} = \frac{Q_N}{4\pi\epsilon_0 r_N} - \frac{Q_{N-1}}{4\pi\epsilon_0} \left( \frac{1}{r_{N-1}} - \frac{1}{r_N} \right) \quad (3.18b)$$

The final expression of the potential is the following:

$$\phi_i = \frac{Q_N}{4\pi\epsilon_0 r_N} - \sum_{j=i}^{N-1} \frac{Q_j}{4\pi\epsilon_0} \left( \frac{1}{r_{j+1}} - \frac{1}{r_j} \right) \quad i = 1, 2, \dots (N-1) \quad (3.19)$$

### 3.3.5 Charge Density

We build a function to estimate charge density.

Because electrons travel at a much greater velocity than ions, they reach distances at which ion density is zero. To appreciate ion and electron density profiles and to compare them, a common sample space interval is used, by uniformly subdividing space between  $\mathcal{R}_{min} = R_{sc}$  and a given  $\mathcal{R}_{max}$ . For each species, the charge density in the generic interval bounded by points  $\mathcal{R}_H$  and  $\mathcal{R}_{H+1}$  is calculated as the product

between the density of computational particle,  $\mathcal{N}/\Delta V$ , and the elementary charge  $q_s$ :

$$\rho_s = \frac{\mathcal{N}_s}{\Delta V} \cdot q_s \quad (3.20)$$

According to the assumption of shell-shaped particles,  $\Delta V = 4/3\pi(\mathcal{R}_{H+1}^3 - \mathcal{R}_H^3)$ .

### 3.4 Shell method convergence study

A convergence analysis of the shell method is performed testing the code with different input parameters. This study is aimed to determine how outputs are sensitive to initial data variation.

This technique is effective to test the robustness of a model and to evaluate the accuracy of results at different numerical grid refinement levels.

The emphasis is placed on two discretization parameters that influence numerical process: time step  $d\tau$  and number of shells emitted at each iteration  $\Delta N_s$ .

If the refinement of solution grid is increased (i.e.  $d\tau$  is reduced and  $\Delta N_s$  rises) and the numerical model approaches to a fixed value, the model is *convergent*.

The code here used simulates the expansion of a Helium plasma in vacuum.

Helium atoms are assumed to be partially ionized, so plasma is composed of electrons and ions  $He^+$ , whose charge is  $|e|$ .

The mass ratio between the two species is  $m_i/m_e = 7344$ .

The shell code is developed using normalized variables; the reference values are  $T_{ref} = 2.3 \text{ eV}$  and  $n_{ref} = 10^4 \text{ cm}^{-3}$ . According to the normalization illustrated in section 2.2.2, input data are grouped below:

Quantity	Value
$\hat{T}_e$	1
$\hat{T}_i$	0.2
$\hat{v}_{drift}$	0.055
$\hat{I}_i$	77.6
$\hat{I}_e$	560
$\tau_c$	1500

Table 3.1: Input data

The adopted numerical method to solve the differential equation of motion (3.2) is the leapfrog integration scheme.

Leapfrog integration is a second-order method that solves Newton’s law equations taking advantage of the decoupling of space and velocity vectors from their derivatives.

The numerical approximation of the system (3.2) employs time-centered finite-differential equations:

$$\mathbf{x}_{n+3/2} = \mathbf{x}_{n+1/2} + \mathbf{v}_{n+1}\Delta t \quad (3.21a)$$

$$\mathbf{v}_{n+1} = \mathbf{v}_n + \frac{q}{m}\mathbf{E}_{n+1/2}\Delta t \quad (3.21b)$$

Since the initial phase space coordinates are  $\mathbf{x}_0$  and  $\mathbf{v}_0$ , at the first iteration ( $n = 0$ ), the quantity  $\mathbf{x}_{n+1/2}$  is not known. It is possible to make a first approximation doing a single Euler half step:

$$\mathbf{x}_{1/2} = \mathbf{x}_0 + \mathbf{v}_0\frac{\Delta t}{2} \quad (3.22)$$

Once the position advances in time, the electric field for  $t = t_0 + \Delta t/2$  can be calculated, and can be used to obtain velocity  $\mathbf{v}_1$  through the equation (3.21b). The leapfrog method is used because it is simple to implement and it has a favorable stability when computing oscillatory solutions [31].

### 3.4.1 Time discretization

First, four simulations in which the time step  $d\tau$  is progressively decreased are evaluated (see table 3.2). The number of shells ejected from the source at each iteration is fixed as  $\Delta N_i = 10$  and  $\Delta N_e = 10$ .

Simulation	Time step $d\tau$
<i>a</i>	0.1
<i>b</i>	0.05
<i>c</i>	0.02
<i>d</i>	0.01

Table 3.2: Input time steps for convergence study

The time step variation has an impact on other quantities of the model. For example, it is noticeable from the equation (3.12) that the charge of a computational particle  $q_s$  is directly proportional to the time step and inversely proportional to the number of shells.

$$q_s \propto \frac{d\tau}{\Delta N_s} \quad (3.23)$$

A change of the elementary charge affects the electric field calculation, and consequently the dynamics of particles.

On the other hand, time steps used for the convergence study diverge by an order of magnitude at most; it is expected that the main quantities of collected simulations to not vary significantly between them.

Decreasing the time step, a smoother profile of potential distribution close to the spacecraft at the end of expansion (figure 3.3b) is exhibited. The asymptotic behaviors do not show a significant difference.

From figures 3.3c and 3.3d, it can be seen that ion density distributions present a negligible difference by refining the time step; the electron charge densities differ for the oscillation amplitude, that is reduced progressively from simulation *a* to simulation *d*.

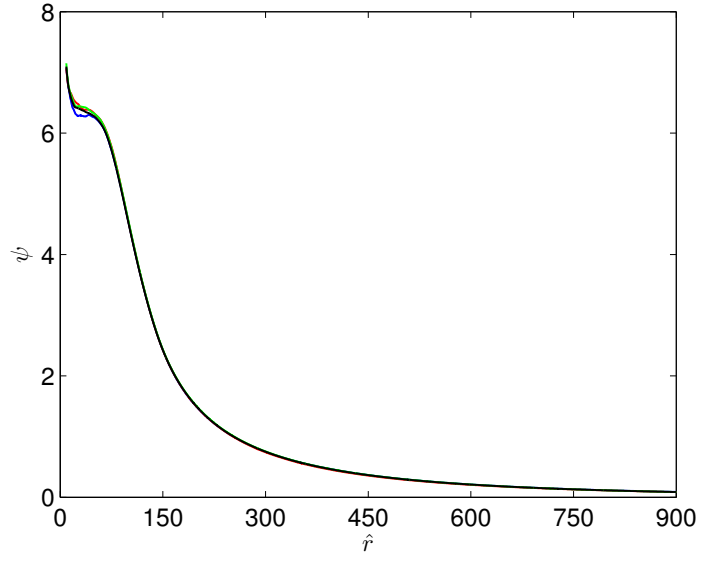
It is evident from figures in 3.3e and 3.3f that quantities depending on charge show oscillations of different magnitude amplitude. After an initial peak, both spacecraft charge and potential settle around an average value; their oscillations are dampened as  $d\tau$  goes down.

It should also be noticed that modifying the time step has a secondary effect on the simulation: the ejections of  $(\Delta N_i + \Delta N_e)$  particles occurs at *each*  $d\tau$ . For this reason, varying the resolution of time discretization, the number of computational shells introduced in the system is modified.

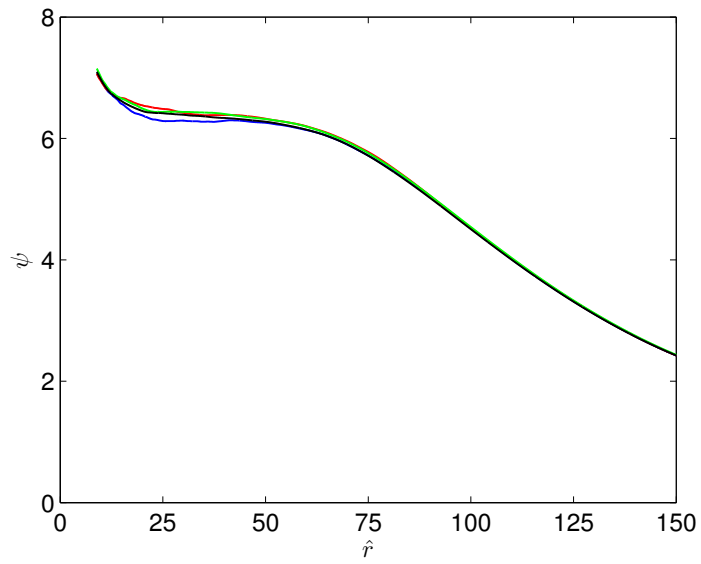
For instance, the results of simulation *d* show a less fluctuating profiles in time and a more uniform distributions in space of quantities of interest, because there are both a greater number of:

- numerical iterations needed to solve differential equations;
- computational particles ejected from the emitter, through which the total charge of the system is represented.

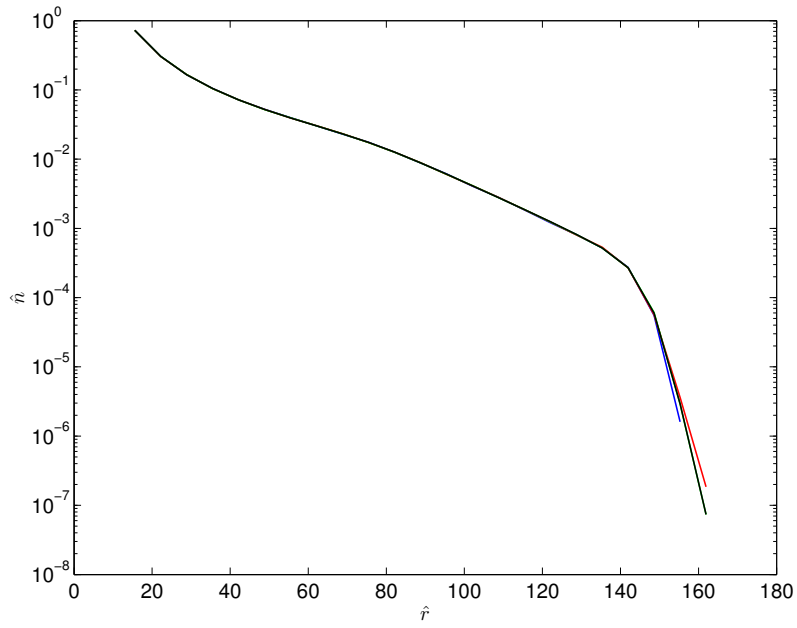
Both effects smooth the curves and reduce the oscillations.



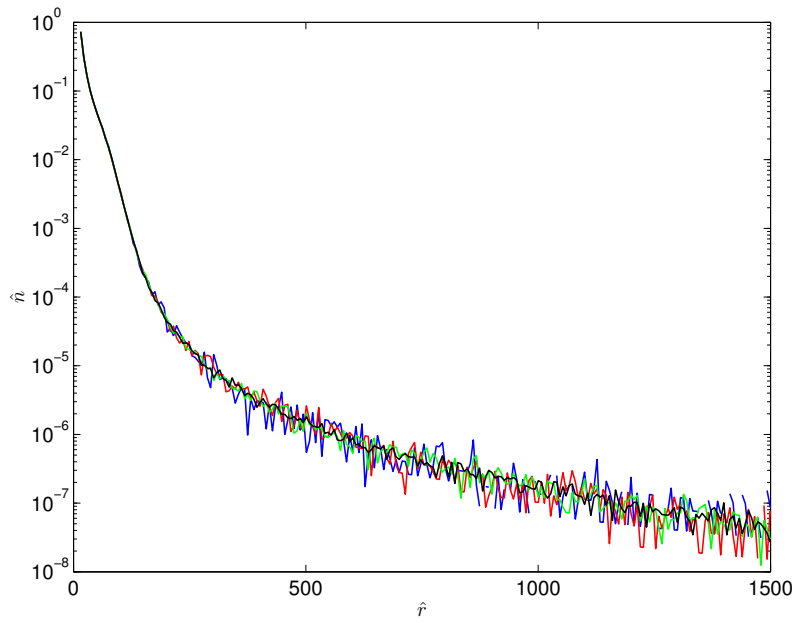
(a) Potential as a function of  $\hat{r}$  at  $\tau_c = 1500$



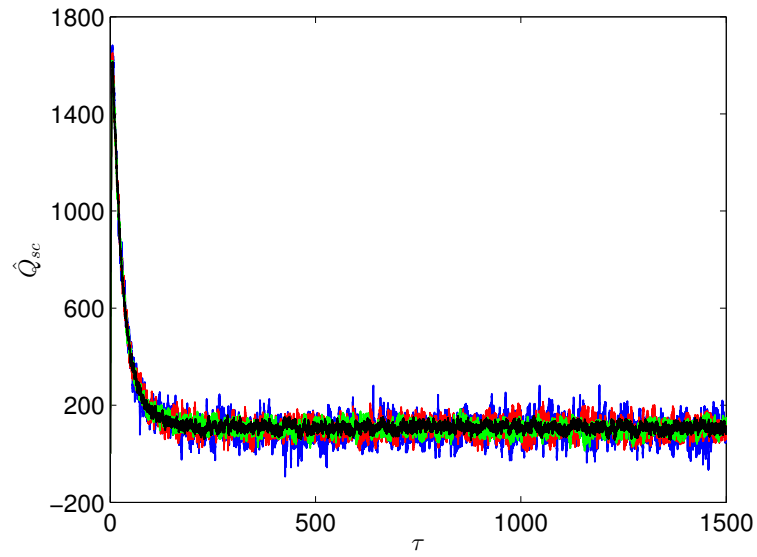
(b) Zoom of potential distribution closer to spacecraft



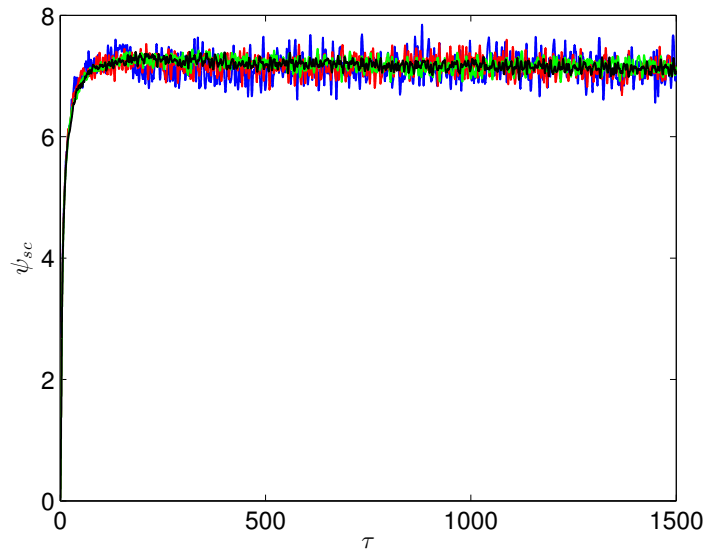
(c) Ion density distribution at  $\tau_c = 1500$



(d) Electron density at  $\tau_c = 1500$



(e) Spacecraft charge time evolution



(f) Spacecraft potential time evolution

Figure 3.3: Convergence study plots varying time step  $d\tau$ :  
 $d\tau = 0.1$  (blue),  $d\tau = 0.05$  (red),  $d\tau = 0.02$  (green),  $d\tau = 0.01$  (black).

### 3.4.2 Number of shells

To establish the influence of the number of shells, it is fixed  $d\tau = 0.01$  and the number of shells is changed, as can be seen in table 3.3.

Simulation	Ion shell number	Electron shell number
1	1	1
2	1	4
3	4	8
4	10	10

Table 3.3: Input number of shells for convergence study

At the end of expansion, potential distributions in space (figures 3.4a and 3.4b) are slightly perturbed for cases in which the sum of computational particles is low. This effect is tempered further away from the spacecraft. Values of density at the end of the transient are very close.

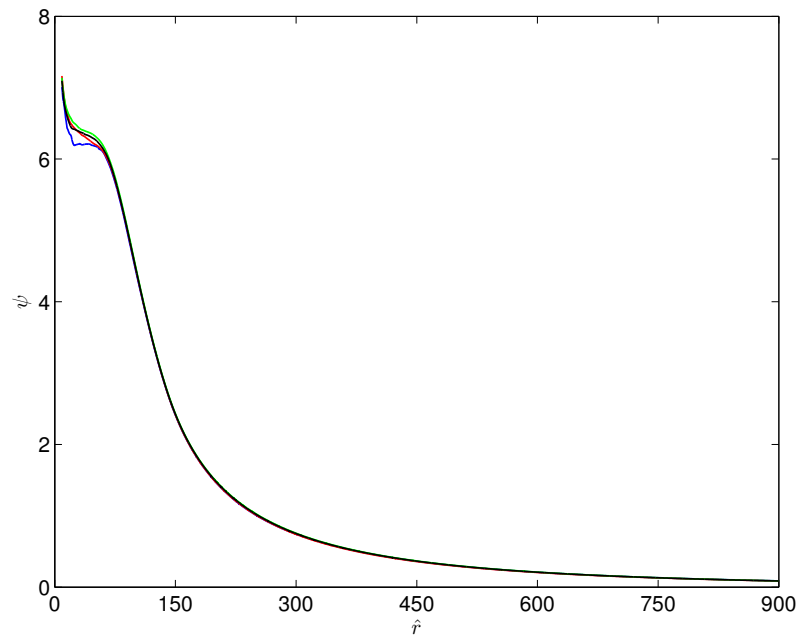
In figures 3.4e and 3.4f, it is clearly shown that oscillations of spacecraft charge and potential are more evident when  $\Delta N_s = 1$ , while their amplitude is gradually reduced by increasing the number of shells.

We give a possible interpretation of the oscillating trend of these two quantities, referring to the simulations 1 and 4, between which  $\Delta N_s$  differs by a factor of 10. In the first simulation, the whole system is represented by a minor number of particles, that are characterized by a bigger elementary charge with respect to the latter case ( $q_s \propto 1/\Delta N_s$ ). Thus, when particles are absorbed by the satellite surface, their 'greater' charge is accumulated on the spacecraft, causing a more significant variation of  $Q_{sc}$ .

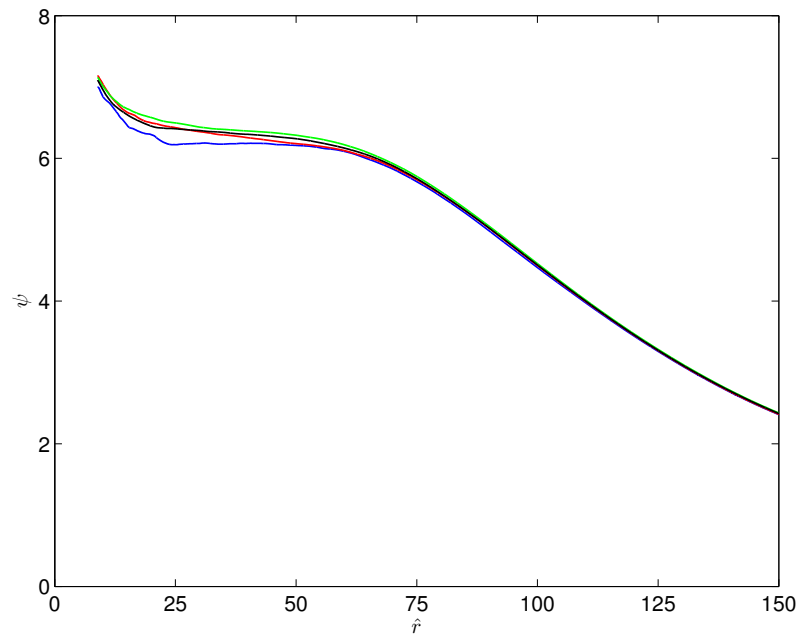
Indeed, in the second instance, the higher number of shells involves in the system more computational particles, whose elementary charge is inferior.

These results confirm that the increase in the number of shells provides an improvement in the solution, comparable to that one obtained through the reduction of  $d\tau$ .

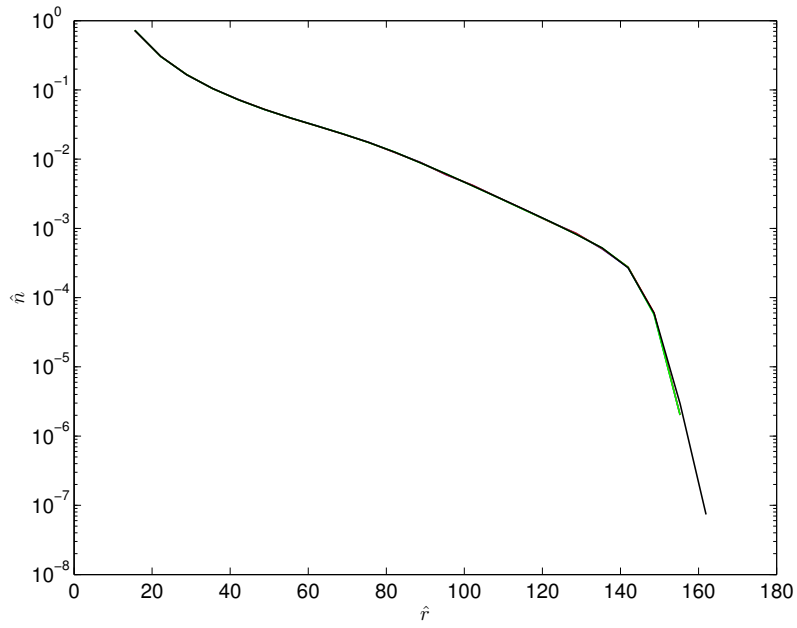
In conclusion, the results obtained from simulations show a convergent trend.



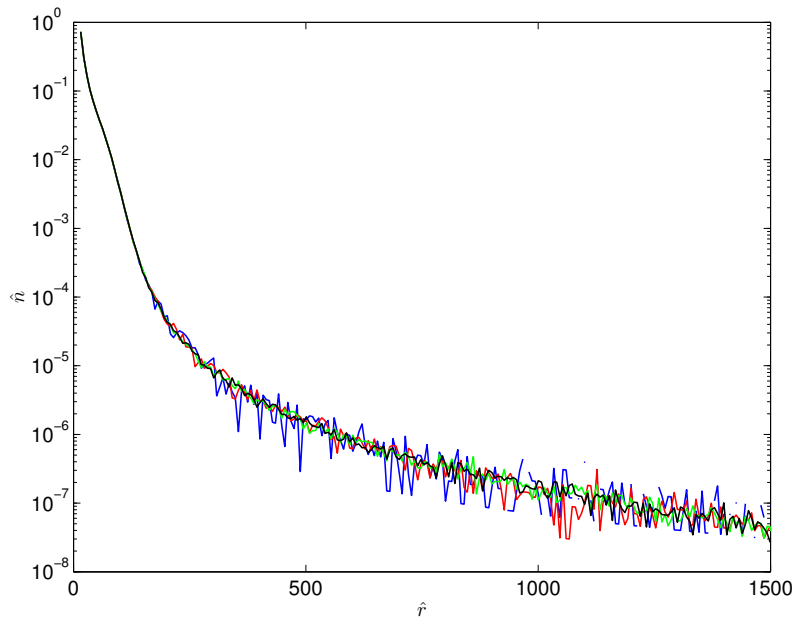
(a) Potential as a function of  $\hat{r}$  at  $\tau_c = 1500$



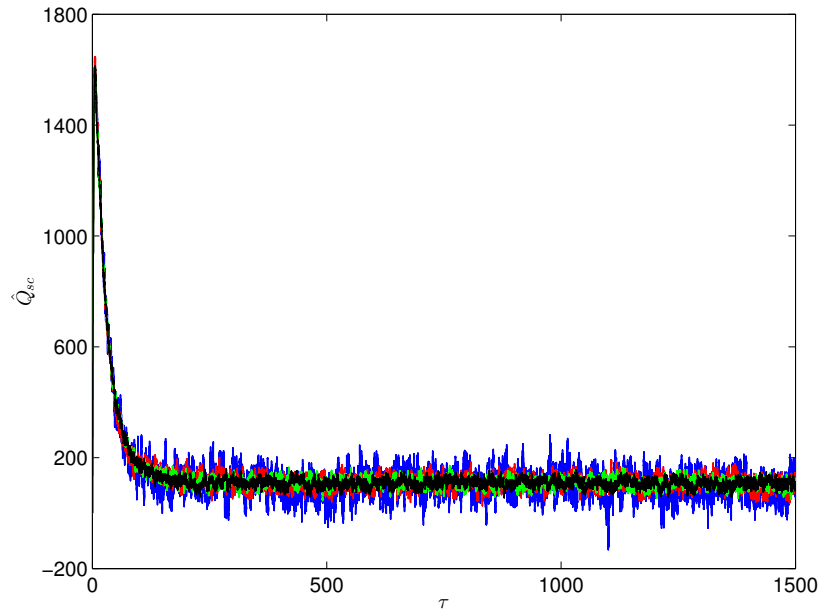
(b) Zoom of potential distribution closer to spacecraft



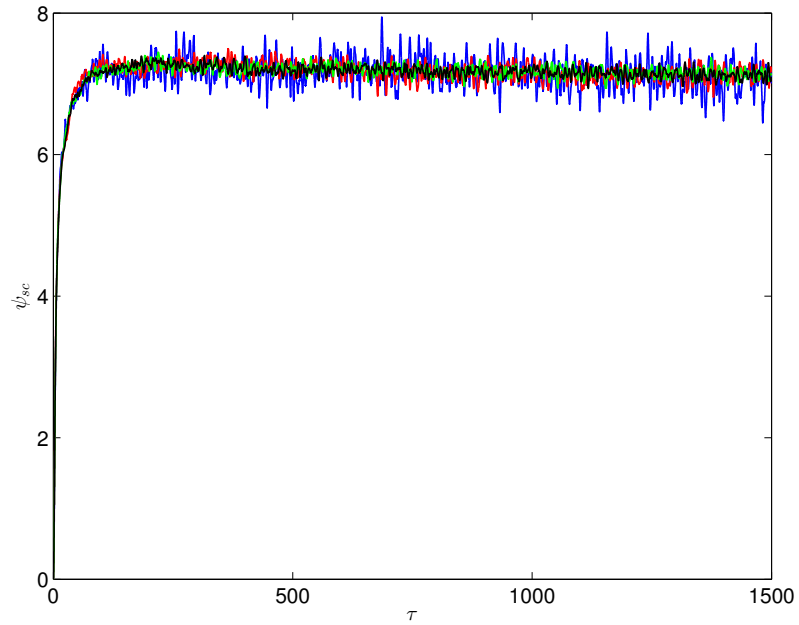
(c) Ion density distribution at  $\tau_c = 1500$



(d) Electron density at  $\tau_c = 1500$



(e) Spacecraft charge time evolution



(f) Spacecraft potential time evolution

Figure 3.4: Convergence study plots varying time step  $\Delta N_s$ : simulation 1 (blue), simulation 2 (red), simulation 3 (green), simulation 4 (black).

### 3.5 CPIC -Shell simulations parallelism

In this section, a comparison between the results from Curvilinear Particle-In-Cell (CPIC) simulation [24] and from shell model presented in section 3.3, for the case of Helium plasma are made.

The reference shell outputs derive from the most refined grid simulation ( $d\tau = 0.01$ ,  $\Delta N_i = 10$  and  $\Delta N_e = 10$ ). Compared outputs are:

- radius of quasi-neutrality cloud surrounding spacecraft  $\hat{r}_{qn}$ ;
- position  $\hat{r}_i$  and velocity of the ion front  $\hat{v}_i$ ;
- potential distributions at the end of expansion (paying attention to values of ion front  $\psi_i$  and spacecraft  $\psi_{sc}$  potentials);
- density distribution in space at  $\tau_c$ .

For the calculation of  $\hat{r}_{qn}$ , it was hypothesized that the quasi-neutrality region ends when the relative difference between ion and electron density  $(\hat{n}_i - \hat{n}_e)/\hat{n}_e$  exceeds the value 0.15 [24], in order to keep the statistical noise of PIC method to acceptable values.

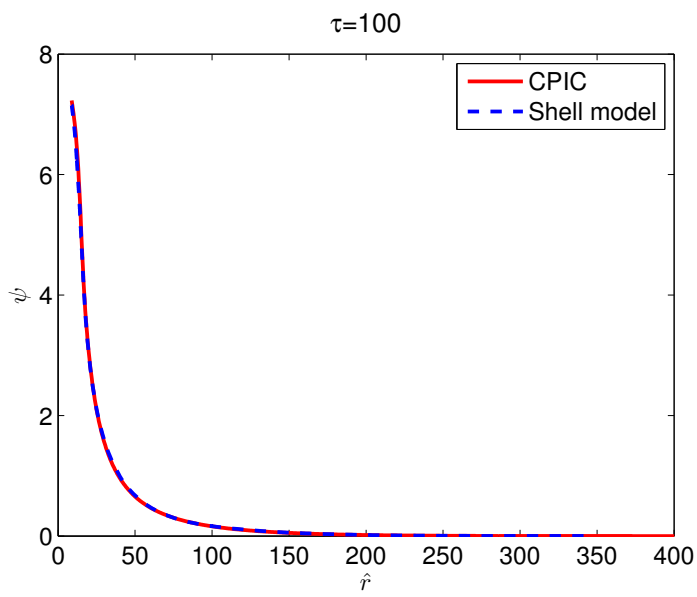
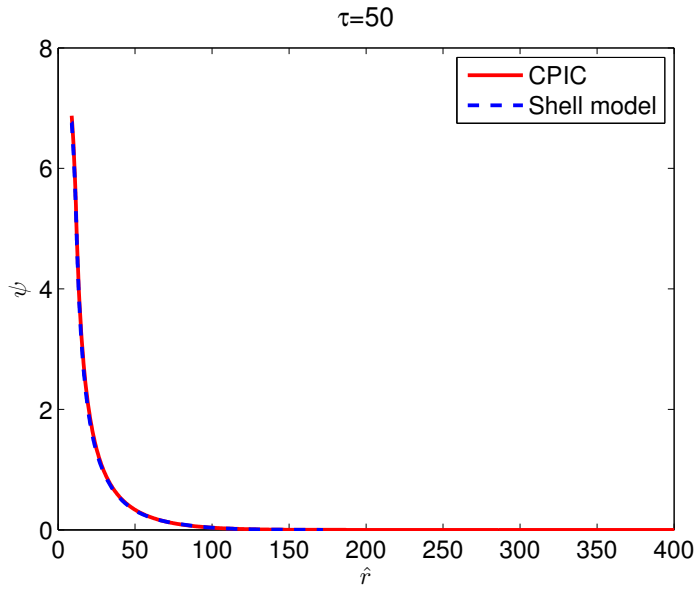
The ion front coordinate is determined by the position of the farthest ion; once  $\hat{r}_i$  is obtained, the values of potential at that point (ion front potential  $\phi_i$ ) and last ion velocity  $\hat{v}_i$  can be extrapolated.

Output variable	CPIC	Shell method
$\hat{r}_{qn}$	65.30	62.12
$\hat{r}_i$	150.96	158.11
$\hat{v}_i$	0.10	0.10
$\psi_i$	2.30	2.21
$\psi_{sc}$	7.39	7.1

Table 3.4: Summary of results in CPIC and shell method simulation

Figures in 3.5 display a positive relationship between the CPIC and shell model, for the entire transient of the expansion.

Figure 3.5a represents the potential distribution in the early stage of system evolution ( $\tau = 50$ ), when particles still have not reached great distances from the spacecraft. The shell model is gridless, so the potential is calculated up to the last particle coordinate; CPIC model contrarily subdivides the domain in meshes.



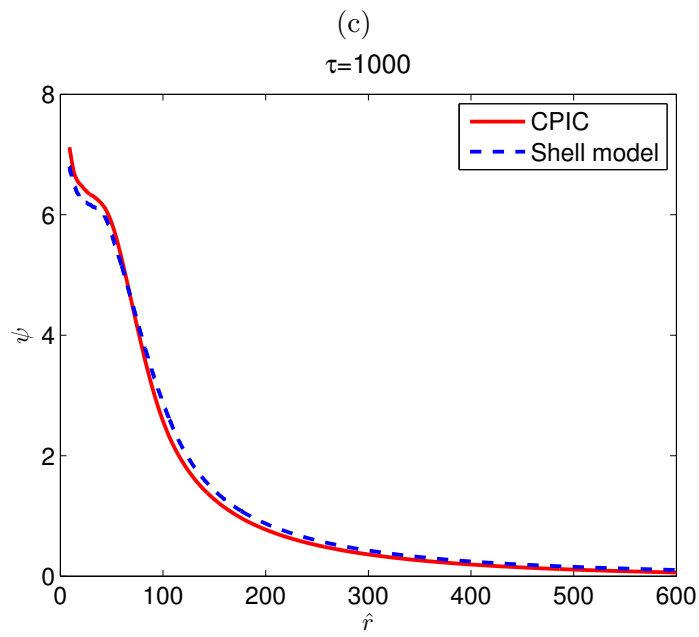
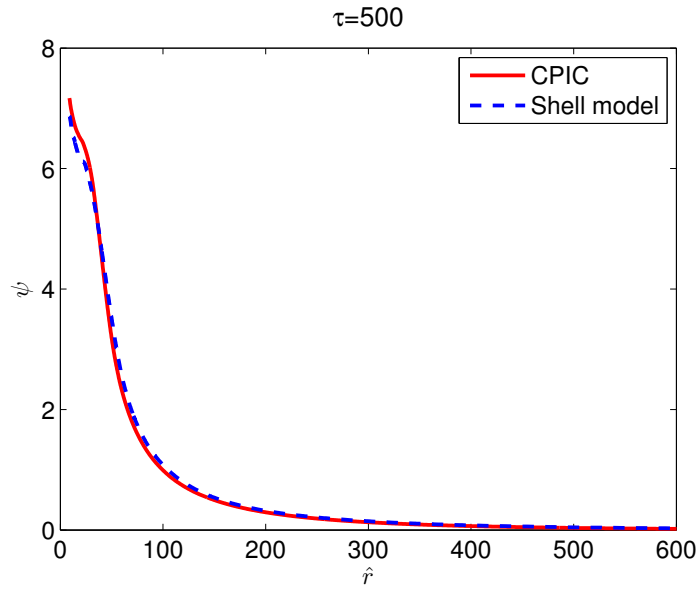


Figure 3.5: Potential space distribution at different time instants before the end of transient.

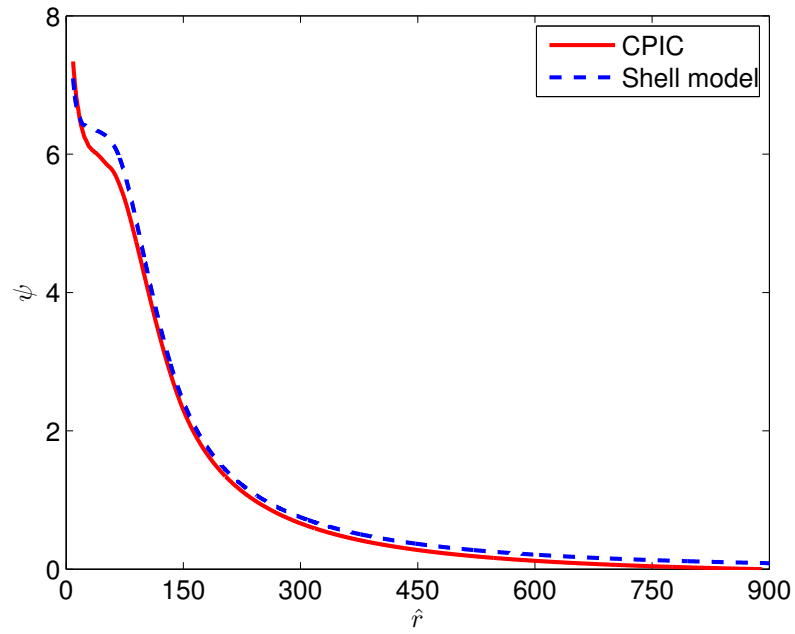


Figure 3.6: Potential distribution in space at the end of expansion  $\tau_c = 1500$ .

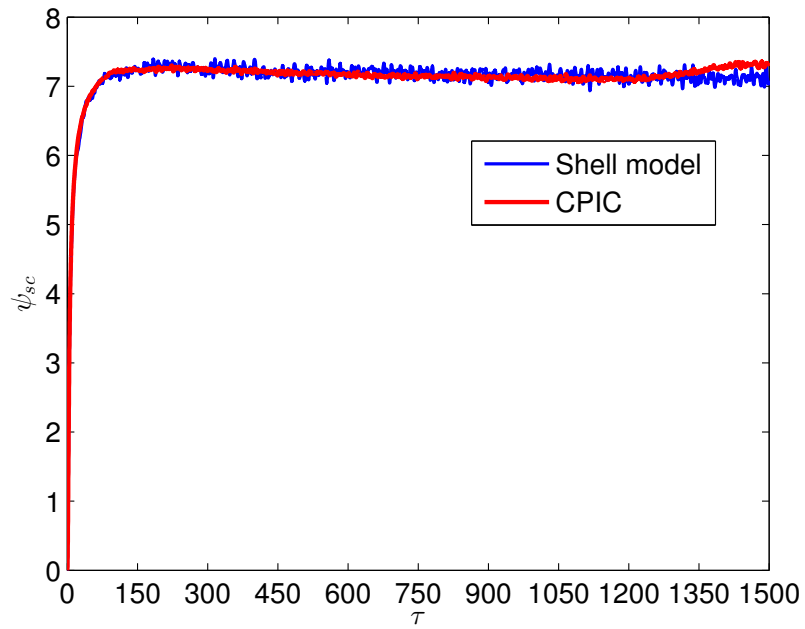


Figure 3.7: Spacecraft potential time evolution.

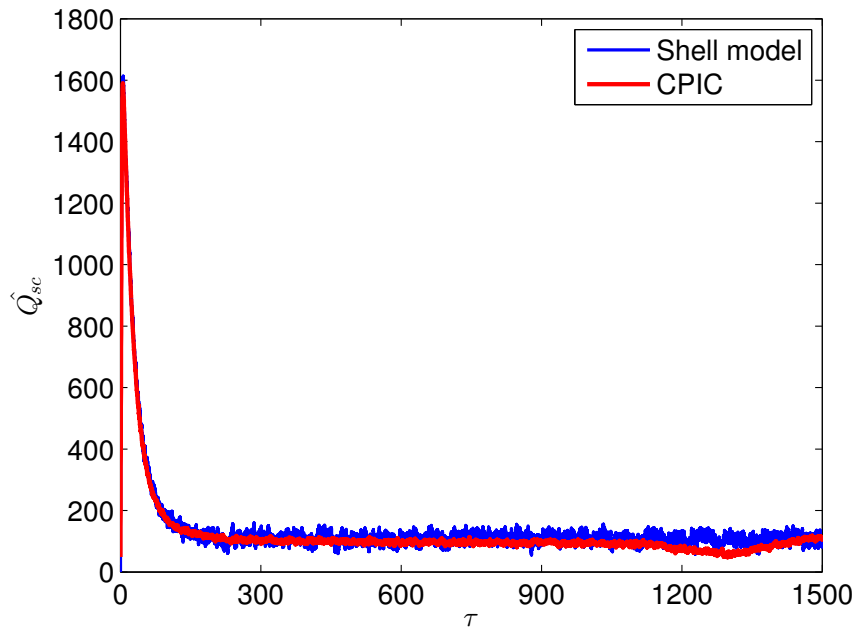


Figure 3.8: Total charge accumulated on the spacecraft.

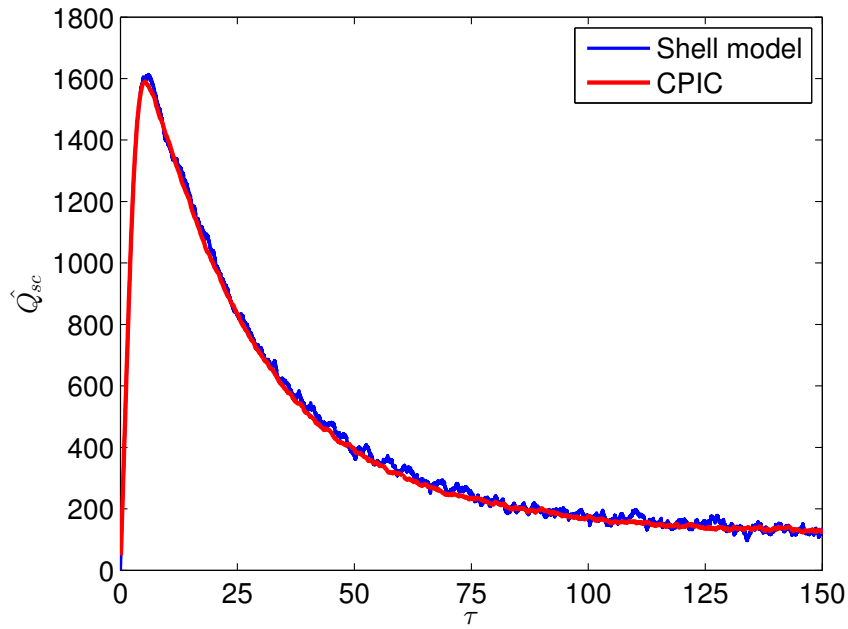


Figure 3.9: Zoom of the figure 3.8 in the first transient instants.

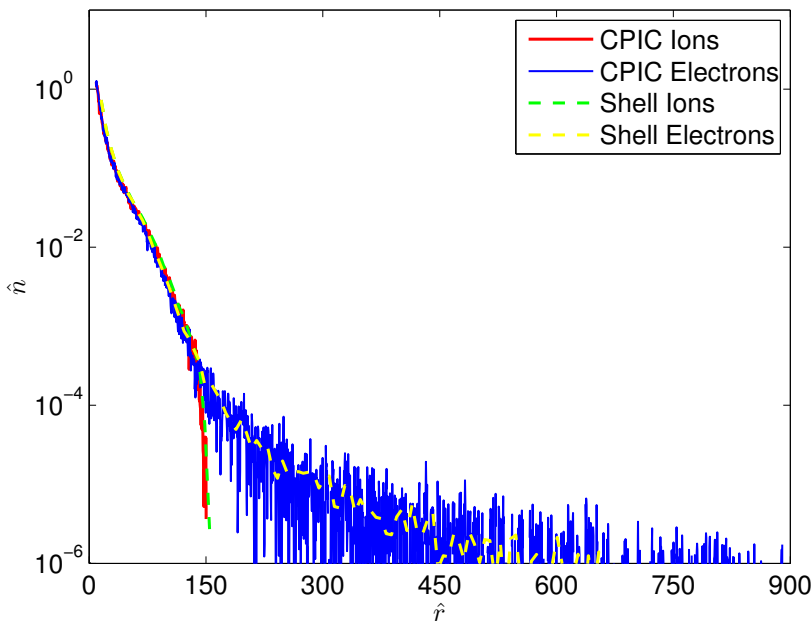


Figure 3.10: Density profiles at the end of expansion  $\tau_c = 1500$ .

The outer boundary of the domain is delimited by the coordinate  $\hat{r}_2 = 900$ , and at every time instant each parameter is calculated on the entire PIC domain. Similarly, later behavior of the system is fully represented by the shell method, that stores coordinates of all particles. The CPIC domain is finite, and when a particle crosses  $\hat{r}_2$ , it is delated from the simulation.

As can be noticed from convergence study graphs (section 3.4), the shell method quantities related to charge manifest oscillating behaviors in time, as opposed to CPIC profiles.

Two interpretations of this result are given: numerical fluctuations can reproduce a physical oscillation of the system charge, whereas electrons moving both back and forth with respect to spacecraft position. On the other hand, the model approximates a continuous ejection of particles with discontinuous and repeated emissions, occurring at each time step. This hypothesis is coherent with the oscillation amplitude attenuation, that is noticeable at a lower temporal discretization. In the latter case, the oscillations are entirely of numerical nature.

In conclusion, we can confirm that shell model is in a good agreement with CPIC, in fact relative errors of quantities compared in table 3.4 are bounded within a maximum of 6 %.

### 3.6 Scaling Law for Spacecraft Potential

A parametric study is performed in order to achieve a scaling law for spacecraft potential.

Spacecraft potential forecasts are paramount from a mission point of view; for this purpose, scaling law is a useful tool because it allows to predict values of this variable as a function of some other significant quantities.

$$\psi_{sc}^{max} = f\left(\frac{m_i}{m_e}, \hat{I}_b, \tau_c\right) \quad (3.24)$$

The spacecraft potential is affected by the variation of contactor ion mass, beam current and contactor expansion time. The dependence relation above contains normalized variables.

The dependency on mass ratio and beam current has been studied in [24]. The results show that:

$$\psi_{sc}^{max} \propto \left(\frac{m_i}{m_e}\right)^{0.35} \quad (3.25a)$$

$$\psi_{sc}^{max} \propto \hat{I}_b^{0.76} \quad (3.25b)$$

Since the beam current is kept equal to the ion contactor current, the variation of  $\hat{I}_b$  implies the variation of  $\hat{I}_i$ .

The dependency of spacecraft potential on  $\tau_c$  is taken into account, simulating the contactor expansion at several times; the contactor is kept on for a time interval on the order of milliseconds.

Simulation	$t_c$ [ms]	$\tau_c$ [-]
$T_1$	5	2.8 e5
$T_2$	10	5.6 e5
$T_3$	20	11.2 e5
$T_4$	50	2.8 e6
$T_5$	100	5.6 e6

Table 3.5: End expansion time inputs

From each simulation, the potential profile in space during the beam emission regime is obtained, solving Poisson equation (2.23) with the initial conditions  $\hat{r}_{qn}$ ,

$\hat{r}_i$ ,  $\hat{v}_i$  and  $\hat{Q}_i$  at the end of expansion. Electron beam is kept on for a time interval of  $\tau_b = 2.5e6$ .

All contactor expansion simulations have been repeated varying the contactor input current, as shown in table 3.6.

Cases	$I_i$ [mA]	$\hat{I}_i$ [-]
<i>I</i>	1	77.6
<i>II</i>	0.1	7.76
<i>III</i>	5	388.2

Table 3.6: Ion contactor current inputs

Output quantities obtained from contactor simulation and used as initial conditions are displayed in tables 3.7, 3.8 and 3.9.

variable	$T_1$	$T_2$	$T_3$	$T_4$	$T_5$
$\hat{r}_{qn}$	1410	2412	4814	12423	23502
$\hat{r}_i$	3016	6191	12682	32627	66552
$\hat{v}_i$	0.1119	0.1145	0.1170	0.1200	0.1221
$\hat{Q}_i$	1.15e5	2.33e5	4.56e5	1.10e6	2.18e6

Table 3.7: Results for case *I*

variable	$T_1$	$T_2$	$T_3$	$T_4$	$T_5$
$\hat{r}_{qn}$	476	1210	2211	5415	10554
$\hat{r}_i$	2644	5403	11014	28175	57259
$\hat{v}_i$	0.0975	0.0993	0.1009	0.1030	0.1045
$\hat{Q}_i$	5.88e4	1.18e5	2.35e5	5.79e5	1.15e6

Table 3.8: Results for case *II*

variable	$T_1$	$T_2$	$T_3$	$T_4$	$T_5$
$\hat{r}_{qn}$	2011	4414	7417	20632	40989
$\hat{r}_i$	3356	6889	14108	36266	72993
$\hat{v}_i$	0.1246	0.1274	0.1300	0.1332	0.1348
$\hat{Q}_i$	1.65e5	2.93e5	5.99e5	1.42e6	2.6e6

Table 3.9: Results for case *III*

An approximation law for the maximum value of the spacecraft potential  $\psi_{sc}^{max}$  is deduced using two functions:

- *power law approximation*

$$\psi_{FIT}^{max} \propto \tau_c^\gamma$$

- *polynomial approximation*

$$\psi_{FIT}^{max} \propto a_1\tau_c^n + a_2\tau_c^{n-1} + \dots + a_n\tau_c + a_{n+1}$$

We fit values of  $\psi_{sc}^{max}$  by the least square method: the approximated function minimizes the sum of the squares of the residual  $\rho_i = |\psi_{sc}^{max} - \psi_{FIT}^{max}|$ .

### 3.6.1 Power law approximation

The first consideration is that  $\psi_{FIT}^{max} = A\tau_c^\gamma$ , where  $A$  is a constant.

Thus, the parametric study in the three cases in table 3.6 is performed in order to verify if and how the dependency of  $\psi_{FIT}^{max}$  as a function of  $\tau_c$  is influenced by  $\hat{I}_i$ .

The results are summarized in table 3.10:

Simulation	$\gamma$	Relative error (%)
<i>I</i>	-0.17	12
<i>II</i>	-0.23	9
<i>III</i>	-0.15	11

Table 3.10: Power law approximation results

### 3.6.2 Polynomial approximation

In this case,  $\psi_{sc}^{max}$  is fitted with a cubic polynomial. The degree of polynomial is chosen according to the number of data points, in such a way the polynomial is unique.

Since the polynomial is badly conditioned, it has been rescaled using the mean  $\mu$  and the standard deviation  $\sigma$  of the vector containing the values of  $\tau_c$  shown in 3.5. Next, we find the coefficients of the polynomial in  $\hat{\tau}_c$ :

$$\hat{\tau}_c = \frac{\tau_c - \mu}{\sigma} \tag{3.26a}$$

$$\psi_{FIT}^{max} = a_1\hat{\tau}_c^3 + a_2\hat{\tau}_c^2 + a_3\hat{\tau}_c + a_4 \tag{3.26b}$$

Simulation	$a_1$	$a_2$	$a_3$	$a_4$	Relative error %
<i>I</i>	-14.45	32.78	-36.54	177.45	0.76
<i>II</i>	-5.76	10.38	-5.23	25.93	7.22
<i>III</i>	-47.40	98.52	-100.65	580.75	4.27

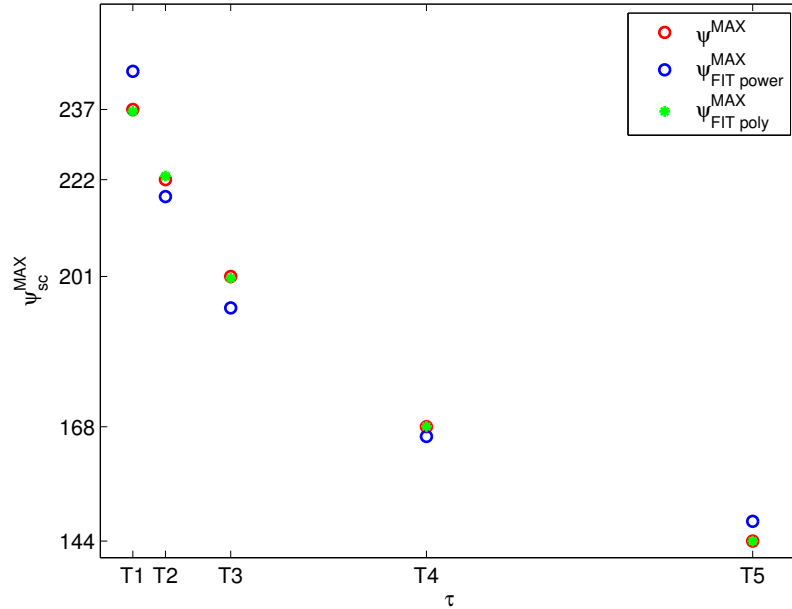
Table 3.11: Polynomial approximation results

The extrapolated coefficients are summarized in table 3.11.

As can be seen from tables 3.10 and 3.11, the polynomial approximation provides more accurate results; at the same time, when the current  $\hat{I}_i$  is changed, polynomial coefficients vary more significantly than the power law  $\gamma$ , whose values are weakly modified.

The power law approximation can be used without taking into account the small variations due to  $\hat{I}_i$ , in order to have a more general and facile applicable relation. A value of  $\gamma = -0.18$  is chosen.

At the end, we can establish that maximum spacecraft potential reached during beam emission regime depends on contactor expansion time prior to beam emission. Increasing time during which contactor plasma expands, weakly reduces the severity of the transient.


 Figure 3.11: Best fit of spacecraft potential values (case *I*).

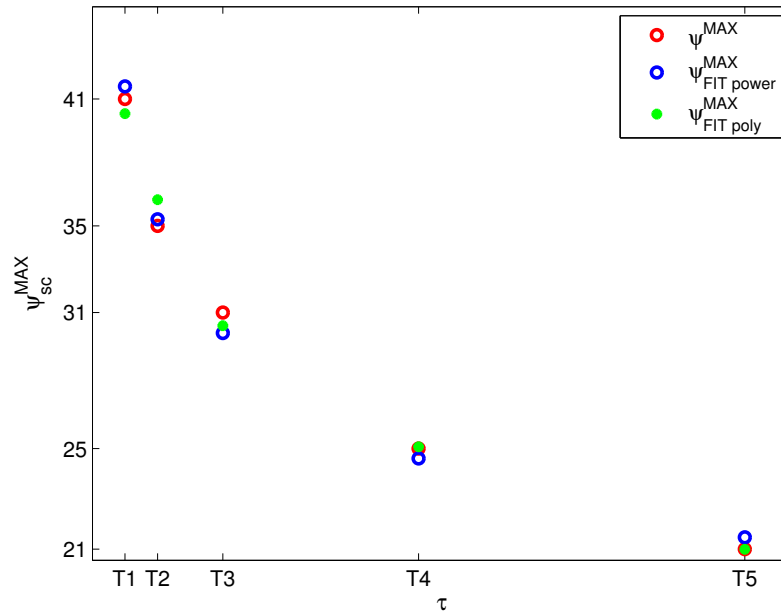


Figure 3.12: Best fit of spacecraft potential values (case *II*).

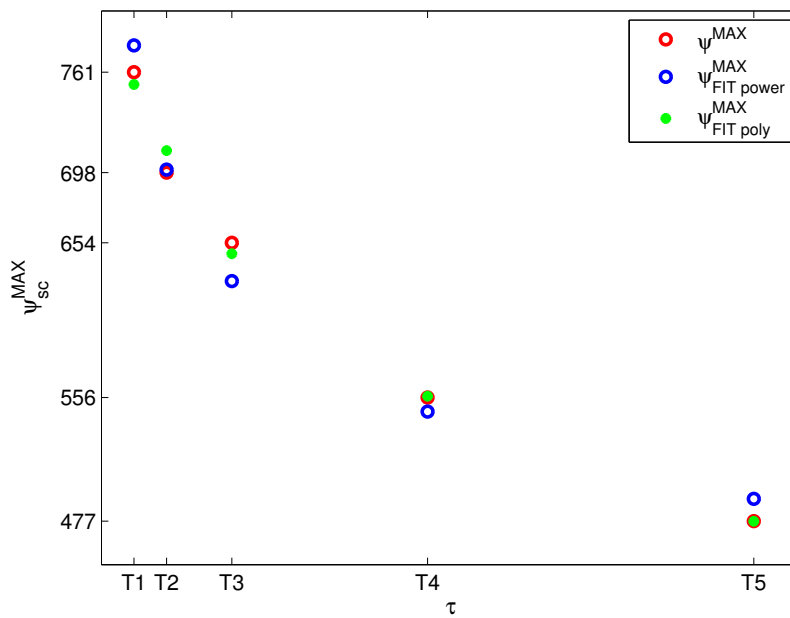


Figure 3.13: Best fit of spacecraft potential values (case *III*).

### 3.7 Shell method for beam emission regime

After the validation of the shell model with a convergence study and its comparison to CPIC simulation, the numerical method is now applied to the second stage of the spacecraft transient: the beam emission regime. The results are compared to the outcomes of the semi-analytical model proposed in [24], which will be referred to as the *base model*.

The electron beam and plasma contactor are fired simultaneously at each time step  $d\tau$ .

Taking advantage of the assumption of infinite-velocity beam, dynamics of electrons fired from the electron gun is ignored, since they instantaneously reach an infinite distance.

The effect of the beam is included in the expression for the spacecraft charge 3.13, that is modified as follows:

$$\hat{Q}_{sc}(\tau) = \hat{Q}_{sc}(\tau - d\tau) - d\hat{Q}_i + |d\hat{Q}_e| + |d\hat{Q}_b| - \left| \sum q_e \right|_{r \leq R_{sc}} \quad (3.27)$$

The beam charge  $d\hat{Q}_b = \hat{I}_b d\tau$ .

The beam current  $\hat{I}_b$  in the present case is equal to the contactor ion current  $\hat{I}_i$ : contactor electron current is assumed to vanish instantaneously (see section 2.2.1). The spacecraft charges positively and its potential increases proportionally with time. Time evolution of spacecraft potential can be seen in figure 3.14.

Contactor electrons are attracted to the spacecraft, and their escape is prevented by the higher attraction force exerted by the satellite.

Contactor ions continue their expansion, reaching, in this regime, distances in which electrons are absent (fig. 3.15).

Finally, the shell method applied to the beam emission regime shows results that are in good agreement with the base model.

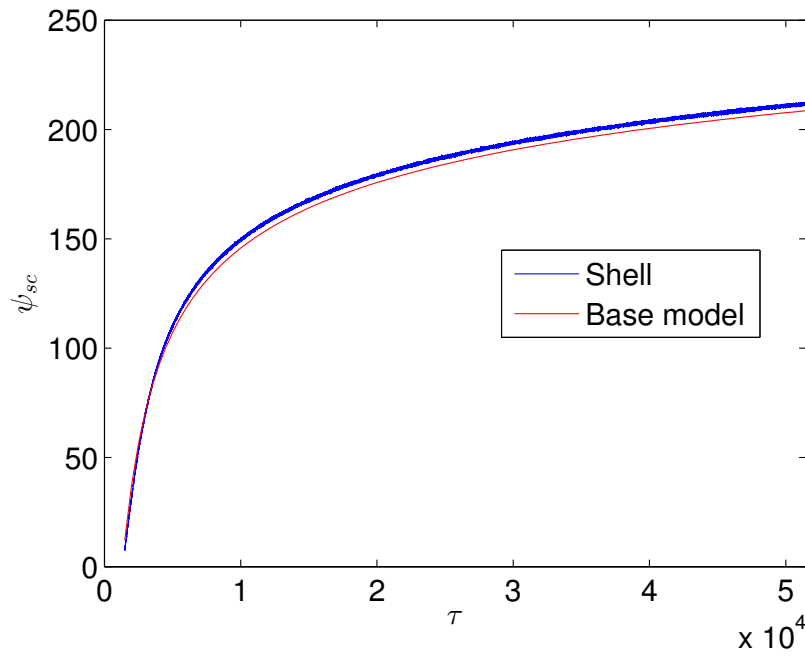


Figure 3.14: Time evolution of spacecraft potential during the beam emission: electron beam is fired at  $\tau_c = 1500$  until  $\tau_b = \tau_c + 50000$ .

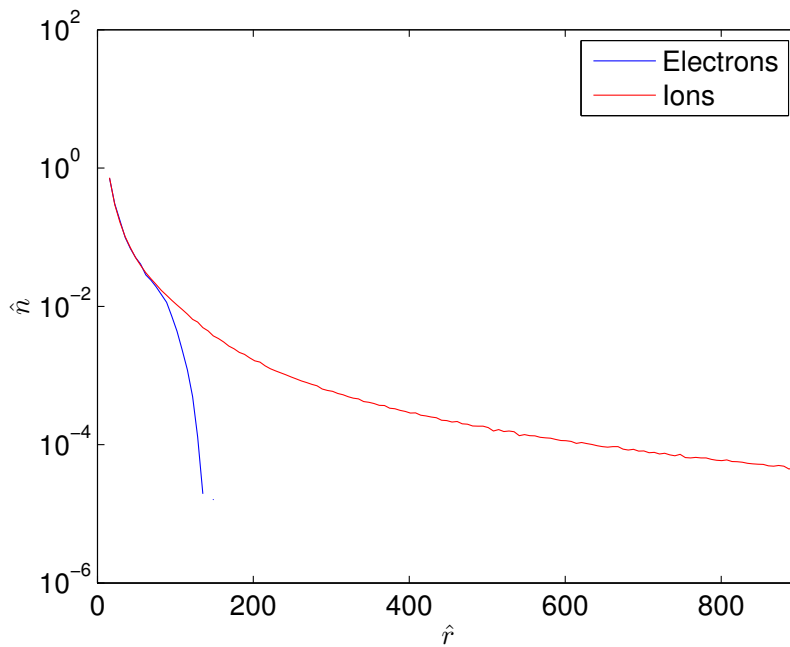
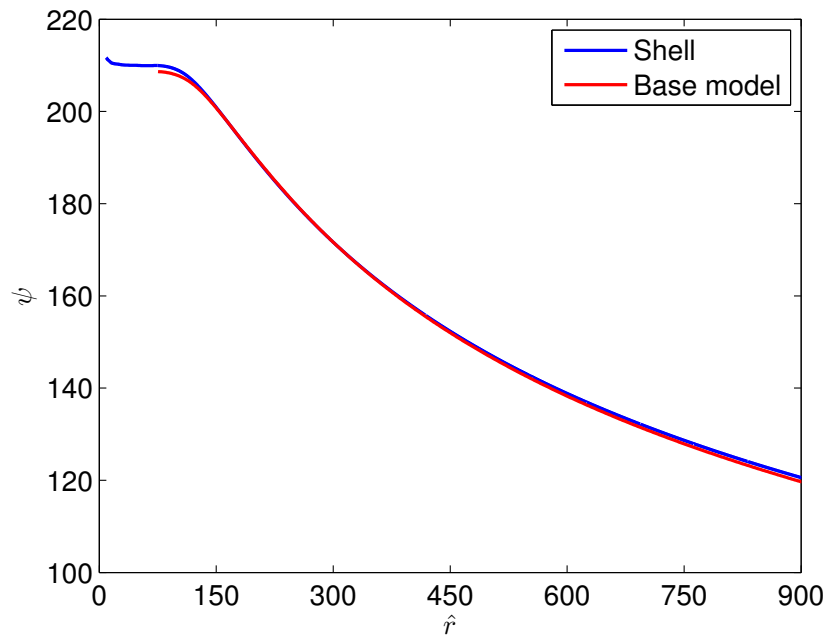


Figure 3.15: Density distribution in space at  $\tau = 11500$ .

Figure 3.16: Potential spatial distribution at the end of the transient  $\tau_b$ .



# Chapter 4

## Semi-analytical model for expansion of contactor plasma

In the current chapter a semi-analytical model under development is introduced. The model expects to be an alternative tool to the shell method to simulate the expansion of a plasma emitted by a source.

### 4.1 Basic assumptions

The fundamental idea behind the development of the semi-analytical model is the decoupling of electron and ion dynamics, since they are characterized by significantly different time scales.

The model equations are referred to a one dimensional radial problem: electrons are assumed to be continuously fired from a spherical source (the spacecraft) with a constant radial velocity  $v_{0e}$ . Electron current  $I_e$  is constant as well. The source emits also ions with a velocity  $v_{0i}$ ; their dynamics is described with the shell approximation. No background magnetic field is considered.

Electron and ion characteristic time scales are proportional to the inverse of electron and ion frequency, so they differ by a factor equivalent to the square root of the mass ratio  $m_e/m_i$  and thus ion motion is the slower process.

On that basis, in the simplified model, the expansion can be partitioned into two phases: in the first, ions are assumed to be static, while electrons reach an equilibrium condition quickly; the second stage is the expansion of ions in vacuum [32]. This phenomenon is influenced by the electric charge distribution developed in the former phase.

The transient proceeds by a time step  $dt$ , after which new particles are ejected and the two-step procedure is repeated.

The numerical method to solve the ion equation of motion takes into account at each iteration a new steady-state distribution of electrons.

The wide separation of time scales improves the computational performances, as the adequate time step to reproduce the expansion accounts for the slower phenomenon only [33].

The suitable time step to follow ion motion is bigger than the time step used in shell simulations, that treat both species dynamics. This advantage is reflected in a reduction of computational time required to reproduce the whole transient.

The potential energy  $U(r)$  is considered zero at the emission point  $r = R_{sc}$ . This is possible because the potential is defined up to a constant. In this case, the total energy is the electron kinetic energy  $\epsilon_{tot} = m_e v_{0e}^2 / 2$ .

For any sequence of electron equilibrium configurations, no quantity depends on time.

If the initial kinetic energy of electrons is sufficiently high to overcome the maximum potential energy, electrons escape indefinitely far away from the spacecraft. In this situation, electron dynamics is not treated; the only effect is on the charge that is carried at infinite distance, which is subtracted by the spacecraft.

Electrons are trapped if at any point of the domain, the potential energy<sup>1</sup> equals the total energy:

$$\frac{m_e v(r)^2}{2} + U(r) = \epsilon_{tot} \quad (4.1a)$$

$$v(r) = \sqrt{\frac{2}{m_e} (\epsilon_{tot} - U(r))} \quad (4.1b)$$

Each particle stops reaching a maximum distance  $r_{max}$  when  $\epsilon_{tot} = U(r_{max})$ , and it comes back toward the spacecraft.

## 4.2 Model equations

For the case in which electrons are trapped, a set of equations is arranged.

It is assumed that the source has a net charge  $Q_{sc}$ . With the exception of the electron current at injection  $I_e$  and the physical constants, all the variables appearing in the following equations are a function of the radial coordinate. For simplicity's sake, in equations' writing, the dependence on  $r$  is omitted.

---

<sup>1</sup>Potential energy value  $U(r)$  derives from both electron and ion contributions.

The fundamental equations of the model are obtained starting from the simplifications made in section 4.1, applied to the Poisson equation in spherical coordinates [34].

$$\frac{1}{r^2} \frac{d}{dr} \left( r^2 \frac{d\phi}{dr} \right) = -\frac{\rho}{\varepsilon_0} \quad (4.2)$$

The total charge density  $\rho$  is the sum of electron and ion density. The equation is rewritten substituting the potential energy  $U = -e\phi$  to the potential.

$$\frac{1}{r^2} \frac{d}{dr} \left( r^2 \frac{dU}{dr} \right) = e \frac{\rho_e + \rho_i}{\varepsilon_0} \quad (4.3)$$

Electron and ion densities are evaluated knowing injection electron current<sup>2</sup> and ion cumulative charge in space  $Q_i$ <sup>3</sup> respectively .

$$\rho_e = \frac{2I_e}{4\pi r^2 v} \quad (4.4a)$$

$$\rho_i = \frac{dQ_i}{dr} \frac{1}{4\pi r^2} \quad (4.4b)$$

The ODE obtained from the Poisson equation with its boundary conditions follows:

$$\left\{ \begin{array}{l} \frac{d}{dr} \left( r^2 \frac{dU(r)}{dr} \right) = \frac{e}{4\pi\varepsilon_0} \left( -\frac{2I_e}{v} + e \frac{dQ_i}{dr} \right) \\ U(R_{sc}) = 0 \\ \left. \frac{dU}{dr} \right|_{r=R_{sc}} = -e \left. \frac{d\phi}{dr} \right|_{r=R_{sc}} = \frac{e}{4\pi\varepsilon_0} \frac{Q_{sc}}{R^2} \end{array} \right. \quad (4.5)$$

Equation 4.5 is valid in the range  $[R_{sc}; r_{max}]$ . The maximum radius reached by electrons is the point in which the velocity is zero ( $v \in [0; v_{0e}]$ ).

To reduce the ODE of second order into two ODEs of first order, we introduce a

---

<sup>2</sup>The corrective factor two is needed since there are a flux of electrons shot from the source and electrons that move back toward it.

<sup>3</sup> $Q_i(r) = \int_{R_{sc}}^r \rho_i(r') 4\pi r'^2 dr'$

new variable  $\Psi$ :

$$\Psi = r^2 \frac{dU}{dr} \quad (4.6)$$

The system of ODEs is defined below.

$$\left\{ \begin{array}{l} \frac{dU}{dr} = \frac{1}{r^2} \Psi \\ U(R_{sc}) = 0 \\ \frac{d\Psi}{dr} = \frac{e}{4\pi\epsilon_0} \left( -\frac{2I_e}{v} + \frac{dQ_i}{dr} \right) \\ \Psi(R_{sc}) = \frac{e}{4\pi\epsilon_0} Q_{sc} \end{array} \right. \quad (4.7)$$

The maximum distance  $r_{max}$  reached by electrons prior to the return toward the spacecraft is not known. To overcome this difficulty, the domain is changed and the problem is inverted:

$$U(r) \rightarrow r(U)$$

Potential energy varies from zero to the total energy value  $U \in [0; \epsilon_{tot}]$ .

Inverting the differential system 4.7, expressions for derivatives of  $r$  and  $\Psi$  with respect to  $U$  have to be found.

$$\frac{d}{dU} = \frac{d\Psi}{dr} \cdot \frac{dr}{dU} = \frac{r^2}{\Psi} \frac{e}{4\pi\epsilon_0} \left( -\frac{2I_e}{v} + \frac{dQ_i}{dr} \right) \quad (4.8a)$$

$$\frac{d\Psi}{dU} = \frac{d\Psi}{dr} \cdot \frac{dr}{dU} = \frac{r^2}{\Psi} \frac{e}{4\pi\epsilon_0} \left( -\frac{2I_e}{v} + \frac{dQ_i}{dr} \right) \quad (4.8b)$$

On the other hands, the system (4.7) has a singularity: the electron velocity  $v = \sqrt{\frac{2}{m_e} (\epsilon_{tot} - U)}$  approaches to zero when  $U \rightarrow \epsilon_{tot}$ . We rewrite the equation:

$$-v \frac{d}{dU} (\Psi) = \frac{r^2}{\Psi} \frac{e}{4\pi\epsilon_0} \left( 2I_e - v \frac{dQ_i}{dr} \right) \quad (4.9)$$

$$- \frac{d}{dU} \left( \sqrt{\frac{2}{m} (\epsilon_{tot} - U)} \cdot \Psi \right) = \frac{r^2}{\Psi} \left( 2I_e - v \frac{dQ_i}{dr} \right) \quad (4.10)$$

We define a new quantity  $p$  such that:

$$-\frac{d}{dU} \left( \sqrt{\frac{2}{m} (\epsilon_{tot} - U)} \right) = \frac{d}{dp} \quad (4.11)$$

Integrating the expression (4.11), it is noticeable that the quantity  $p$  is the momentum  $m_e v$ .

Finally, the radial coordinate  $r$  and the quantity  $\Psi$  are function of  $p \in [0; m_e v_{0e}]$ .

$$\left\{ \begin{array}{l} \frac{dr}{dp} = -\frac{p}{m} \frac{r^2}{\Psi} \\ r(p_0) = R \\ \frac{d\Psi}{dp} = \frac{r^2}{\Psi} \frac{e}{4\pi\epsilon_0} \left( 2I_e - \frac{p}{m} \frac{dQ_i}{dr} \right) \\ \Psi(p_0) = \frac{e}{4\pi\epsilon_0} Q_{sc} \end{array} \right. \quad (4.12)$$

The resolution of the system 4.12 provides the position for both electrons and ions within  $r_{max}$ , and the quantity  $\Psi$ , equivalent to the electric field flux  $\Phi_E$ , multiplied by a constant.

$$\Psi = r^2 \frac{dU}{dr} = er^2 E \quad (4.13a)$$

$$\Phi_E = 4\pi E = \frac{Q}{\epsilon_0} \quad (4.13b)$$

$$\Psi = \frac{e}{4\pi} \Phi_E \quad (4.13c)$$

$Q$  is the cumulative charge at  $r$ .

Since  $\Psi$  allows quantitative knowledge of the electric field, the total charge at each position  $r$  is known as well. In order to solve the ion equation of motion, the electric field is interpolated on ion coordinates  $r_i$ .

### 4.2.1 Numerical example

We provide a numerical example of the described model. The simulation reproduces the expansion of a helium plasma emitted by a charged space probe, during the phase in which electrons are trapped. The spacecraft charge  $Q_0$  at the first time instant is greater than zero; this charge can be regarded as the positive charge arisen on the spacecraft when a neutral satellite emits electrons and ions with a current  $I_e > I_i$ : at early stage, faster electrons have a kinetic energy higher than the potential and escape. After that negative particles leave the spacecraft, its charge increases; the potential rises as well, and electrons are trapped when  $m_e v_{0e}^2/2 \leq |U(r)|$ . Normalized input data are shown in table 4.1.

Quantity	Value
$\hat{v}_{0e}$	0.5
$\hat{v}_{0i}$	0.05
$\hat{I}_e$	1
$\hat{I}_i$	0.5
$\hat{Q}_0$	800
$\tau_c$	1500
$d\tau_m$	5

Table 4.1: Input data of numerical example

The results of the semi-analytical model and shell method have been compared. In the shell model, since both species dynamics are followed, the chosen time step is one hundred times smaller than  $d\tau_m$ . During the transient, electrons surround the spacecraft and some of them are absorbed, decreasing the satellite charge (figure 4.1); ions are repulsed from the positively charged spacecraft and expand ahead of electrons.

In figures 4.2 and 4.3, profiles of quantities as density and potential at the end of transient exhibit a very good accord with the shell model.

It clearly appears that the separation of electron and ion time scales, considering electrons in a sequence of equilibrium states, might be a valuable approximation to describe the physics of the plasma expansion.

Furthermore, this model allows to use a bigger time step, reducing the computational time needed for the numerical simulations. In the present example, the time spent to run the code is reduced of about two orders of magnitude with respect to shell code. This advantage is a strength of the model, that can replace shell method to simulate longer transients.

The obtain results suggest that wider applications of the model can be advanced. Further developments of this theory may be the subject of a future work.

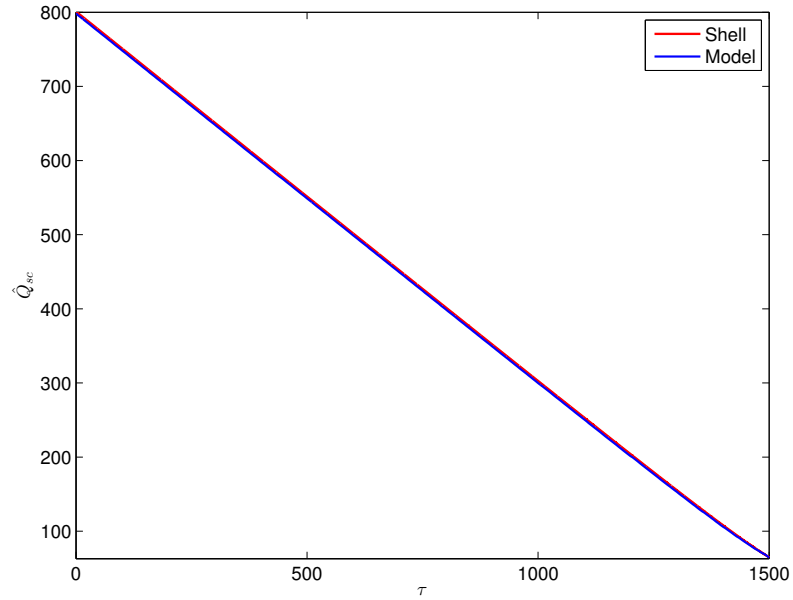


Figure 4.1: Charge accumulated on the spacecraft in time.

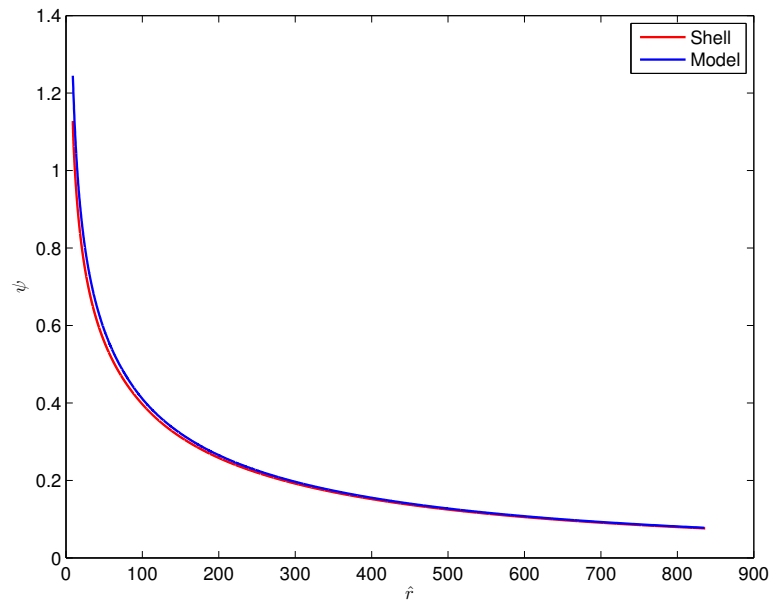


Figure 4.2: Potential distribution in space at the end of expansion  $\tau_c = 1500$ .

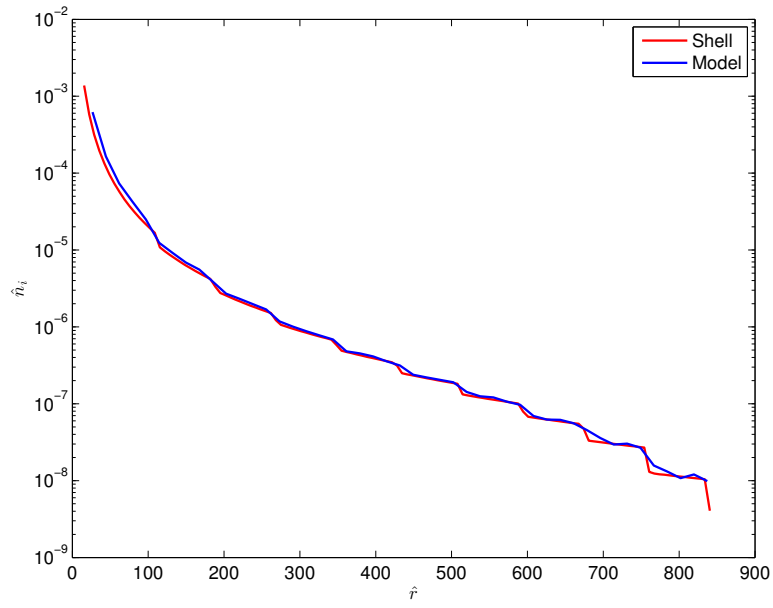


Figure 4.3: Ion density profile in space at the end of expansion  $\tau_c = 1500$ .

# Chapter 5

## Conclusions

In the present work, the plasma contactor technology has been examined as a mitigation configuration for a spacecraft equipped with an electron gun.

In the first place, plasma contactor expansion has been modeled using the numerical shell method.

The shell model has been tested under a set of different input values, in order to determine the effect on its outputs and to evaluate its accuracy behavior. In addition, the obtained quantities of interest have been compared to CPIC simulations, showing convergent trends. After the validation of the shell method, the model has been employed to predict the system behavior under new experimental conditions, deriving a scaling law for the spacecraft potential.

The study conducted with this numerical approach, is accompanied by the analysis of an additional semi-analytical model, currently under development.

Since a long-lasting contactor expansion prior to the beam emission will reduce the magnitude of the transitory, one of the main interest in the contactor expansion study is investigating the responses of the system to longer transients. Faster simulation tools are required, and the semi-analytical model appears to be promising for this purpose.

A further step in this research field might be removing some of the simplifying assumptions that have been made. One example is the study of the phenomenon considering the contribution of a background plasma. Furthermore, we can neglect the assumption on the spherical symmetry at the ejection point: in practice the emission of the plasma occurs on a limited area of the spacecraft. A potential comparison between cases ruled by different hypotheses is helpful to judge wheter approximated solutions can fairly describe an injection profile and be used in real applications.

Finally, the model can be examined in contrast to results of ongoing experiments testing ion emission technique, to ultimately confirm its range of validity and applicability.



# Bibliography

- [1] M.C. Kelley, *The Earth's Ionosphere*, Elsevier Science (2012).
- [2] S.T. Lai, *Fundamentals of Spacecraft Charging: Spacecraft Interactions with Space Plasmas*, Princeton University Press (2011).
- [3] Y. Kamide, W. Baumjohann, *Magnetosphere-Ionosphere Coupling*, Springer-Verlag Berlin Heidelberg (1993).
- [4] G.L. Delzanno, J.E. Borovsky, M.F. Tomsen, B.E. Gilchrist, E. Sanchez, *Can an electron gun solve the outstanding problem of magnetosphere-ionosphere connectivity?*, Journal of Geophysical Research: Space Physics (2016), doi:10.1002/2016JA022728.
- [5] [https://www.nasa.gov/mission\\_pages/sunearth/aurora-news-stories/index.html](https://www.nasa.gov/mission_pages/sunearth/aurora-news-stories/index.html)
- [6] J.E. Borovsky, D.J. Mc Comas, M.F. Thomsen, J.L. Burch, J. Cravens, C.J. Pollock, T.E. Moore, S.B. Mende, *Magnetosphere-Ionosphere Observatory (MIO): A multisatellite mission designed to solve the problem of what generates auroral arcs*, Eos Trans. AGU, Vol. 79 (45), F744 (2000).
- [7] H.B. Garrett, A.C. Whittlesey, *Guide to Mitigating Spacecraft Charging Effects*, Wiley (2012).
- [8] <https://web.archive.org/web/20131231000203/http://gcmd.nasa.gov/add/ancillaryguide/platforms/orbit.html>
- [9] S.T. Lai, *An overview of electron and ion beam effects in charging and discharging of spacecraft*, IEEE Trans. Nuclear Science, Vol. 36, no. 6, p. 2027 (1989).
- [10] G.L. Delzanno, J.E. Borovsky, M.F. Tomsen, D. Moulton, *Future beam experiments in the magnetosphere with plasma contactors: The electron collection and ion emission routes*, Journal of Geophysical Research: Space Physics (2015),

doi:10.1002/2014JA020683.

- [11] H. Mott-Smith, I. Langmuir, *The Theory of Collectors in Gaseous Discharges*, Physical Review, 28, 727 (1926).
- [12] G.L. Delzanno, X.-Z. Tang, *Dust-Plasma Interaction: a review of dust charging theory and simulation*, in *Plasma Modeling: methods and Applications*, edited by G. Colonna, A. D'Angola, chap. 13, pp.13.1-13.26, IOP Plasma Physics Series (2016).
- [13] Z. Nemecek, J. Safrankova, L. Prech, J. Simunek, J. Smilauer, K.I. Gringauz, N.M. Shutte, M.V. Teltsov, B.V. Marjin, Y.Y. Ruzhin, V.S. Dokukin, *Artificial electron and ion beam effect: Active Plasma Experiment*, Journal of Geophysical Research, Vol. 102, no. A2, pp. 2201–2211 (1997).
- [14] R.A. Hendrickson, R.W. McEntire, J.R. Winckler, *Echo 1: An experimental analysis of local effects and conjugate return echoes from an electron beam injected into the magnetosphere by a sounding rocket*, Planet. Space Sci., Vol. 23, pp. 1431-1444 (1975).
- [15] G. Jaffé, *On the Currents Carried by Electrons of Uniform Initial Velocity*, Vol. 65, pp. 91-98, Physical Review (1944).
- [16] C.D. Child, *Discharge from hot CaO*, Vol. 32, pp. 492–511, Physical Review (1911).
- [17] I. Langmuir, *The effect of space charge and residual gases on thermoionic currents in high vacuum*, Vol. 2, pp. 450–486, Physical Review (1913).
- [18] G.L. Delzanno, J.E. Borovsky, M.F. Tomsen, D. Moulton, E.A. MacDonald *Future beam experiments in the magnetosphere with plasma contactors: How do we get the charge off the spacecraft?*, Journal of Geophysical Research: Space Physics ( 2015), doi:10.1002/2014JA020608.
- [19] R.C Olsen, *Experiments in charge control at geosynchronous orbit - ATS-5 and ATS-6*, Vol. 22, No. 3, pp. 254-264, Journal of Spacecraft and Rockets (1985), doi:10.2514/3.25742.
- [20] R. Schmidt et al., *Results from active spacecraft potential control on the Geotail spacecraft*, Vol. 100, No. A9, pp. 17,253–17,259 Journal of Geophysical Research (1995).

- [21] R.H. Comfort, T.E. Moore, P.D. Craven, C.J. Pollock, F.S. Mozer, W.S. Williamson, *Spacecraft potential control by the Plasma Source Instrument on the POLAR satellite*, Vol. 35, No. 6, Journal of Spacecraft and Rockets (1998).
- [22] G.D. Reeves, *CONNEX: The Magnetosphere-Ionosphere Connection Explorer*, COSPAR 3rd Symposium on Small Satellites, Jeju, Korea South (2017).
- [23] E.E. Dors, E.A. MacDonald, L.E. Kepko, J.E. Borovsky et al., *CONNEX: Concept to Connect Magnetospheric Physical Processes to Ionospheric Phenomena*, Active Experiments in Space: Past, Present and Future Workshop, Sante Fe, NM (2017).
- [24] F. Lucco Castello, G.L. Delzanno, J.E. Borovsky, G. Miars, O. Leon, B.E. Gilchrist, *Spacecraft-charging mitigation of a high-power electron beam emitted by a magnetospheric spacecraft: Simple theoretical model for the interpretation of the transient of the spacecraft potential*, Journal of Geophysical Research (2018), doi:10.1029/2017JA024926:
- [25] E. Camporeale, E.A. Hogan, E.A. MacDonald, *Approximate semi-analytical solutions for the steady-state expansion of a contactor plasma*, Plasma Sources Science and Technology (2015), doi:10.1088/0963-0252/24/2/025014.
- [26] E. Boella, G. Coppa, A. D'Angola, B. Peiretti Paradisi, *Gridless particle technique for the Vlasov-Poisson system in problems with high degree of symmetry*, Computer Physics Communication (2017).
- [27] A. D'Angola, E. Boella, G. Coppa, *On the applicability of standard kinetic theory to the study of nanoplasmats*, Physics of Plasmas (2014), doi:10.1063/1.4894109.
- [28] G.W. Collins II, *The foundation of Celestial Mechanics*, Ch.5, pp 61, Case Western Reserve University (2004)
- [29] K.L. Cartwright, J.P. Verboncoeur, C.K. Birdsall, *Loading and Injection of Maxwellian Distributions in Particle Simulations*, Journal of Computational Physics (2000), doi:10.1006/jcph.2000.6549.
- [30] J.E. Crow, P.L. Auer, J.E. Allen, *The expansion of a plasma into a vacuum*, Vol.14, part 1, pp.65-76, Journal of Plasma Physics (1975).

- [31] C.K. Birdsall, A. B. Langdon, *Plasma Physics via Computer Simulations*, Chap. 4, McGraw-Hill Book Company (1985).
- [32] G. Coppa, A. D'Angola, R. Mulas, *A simple model for the dynamics of the electrons in a spherical plasma irradiated by a laser pulse*, *Mathematical and Computer Modelling* 54 2479–2485 (2011).
- [33] G. Coppa, L.O. Silva, A. D'Angola, F. Peano, F. Peinetti, *The ergodic method: plasma dynamics through a sequence of equilibrium states*, Chap. 5, *Plasma Modeling Methods and Applications* (2016).
- [34] G. Coppa, R. Mulas, *Study on the emission of electrons by a spherical object: dynamics of trapped particles* (2018), to be published.

# Ringraziamenti

Desidero ringraziare Gianni e Roberta, che mi hanno seguito con pazienza e costanza in questo lungo lavoro, da vicino e a distanza.

Un ringraziamento particolare va al laboratorio di Los Alamos per avermi ospitata e per avermi dato le risorse necessarie per sostenere questo periodo all'estero. Grazie a Gian Luca, con il quale ho avuto un primo approccio al mondo della ricerca. Questa esperienza è stata formativa non solo dal punto di vista professionale, ma anche umano.

Ringrazio la mia famiglia per avermi supportato (a suo modo), ma ringrazio soprattutto Sara, che ha sempre creduto in me anche quando non avevo io stessa alcuna fiducia.

Un caro ringraziamento ai miei svariati amici e colleghi, specialmente alla mia più accesa sostenitrice, il cui nome merita senz'altro di comparire tra queste righe, Tiffany.

Ultimo in ordine cronologico, ma non per importanza, ringrazio Jarin, con il quale ho riscoperto l'amore.